Ab Initio Studies On The Transport Properties Of High Energy Density(HED) Plasmas

by

Yanhao Ding

Submitted in Partial Fulfillment of the

Requirements for the Degree

Doctor of Philosophy

Supervised by Professor John C. Lambropoulos

Department of Mechanical Engineering

Arts, Sciences and Engineering

Edmund A. Hajim School of Engineering and Applied Sciences

University of Rochester

Rochester, New York

2020

Table of Contents

Biographical Sketch

The author was born in China. He attended Harbin Institute of Technology, and graduated with a Bachelor and Master of Science degree in Mechanical Engineering. He began doctoral studies in Mechanical Engineering at the University of Rochester in 2015. He pursued his research in Department of Mechanical Engineering under the direction of Prof. John C. Lambropoulos.

The following publications were a result of work conducted during doctoral study at University of Rochester.

Peer Reviewed Publications :

1. **Y. H. Ding**, A. J. White, S. X. Hu, O. Certik, and L. A. Collins, *Ab Initio* Studies on the Stopping Power of Warm Dense Matter with Time-Dependent Orbital-Free Density Functional Theory", *Phys.Rev.Lett.* **121**, (145001) (2018).

2. Alexander J. White, Ondrej Certik, **Y. H. Ding**, S. X. Hu, and Lee A. Collins, Time-dependent orbital-free density functional theory for electronic

stopping power: Comparison to the Mermin-Kohn-Sham theory at high temperatures", *Phys. Rev. B* **98**, (144302) (2018).

3. S. X. Hu, L. A. Collins, T. R. Boehly, **Y. H. Ding**, P. B. Radha, V. N. Goncharov, V. V. Karasiev, G. W. Collins, S. P. Regan, and E. M. Campbell, A review on *Ab Initio* studies of static, transport, and optical properties of polystyrene under extreme conditions for inertial confinement fusion applications", *Phys. Plasmas* **25**, (056306) (2018).

4. J. A. Gaffneya, *et al.* [including **Y. H. Ding**], A Review of Equation-of-State Models for Inertial Confinement Fusion Materials", *High Energy Density Physics* **28**, (7-24) (2018).

5. **Y. H. Ding**, and S. X. Hu, First-principles equation-of-state table of beryllium based on density-functional theory calculations", *Phys. Plasmas* **24**, (062702) (2017).

Conferences / Presentations:

1. **Y. H. Ding**, A. J. White, S. X. Hu, O. Certik, and L. A. Collins, Ab-initio Studies on the Stopping Power of Warm Dense Matter with Time- Dependent Orbital Free Density Functional Theory *60th APS DPP.*, Portland, Oregon

2. **Y. H, Ding**, S. X. Hu, Density-Functional-Theory–Based Equation-of-State Table of Beryllium for Inertial Confinement Fusion Applications *59th APS DPP.*, Milwaukee, WI

3. **Y. H, Ding**, S. X. Hu, First-principles equation-of-state table of beryllium for High-Energy-Density Plasma Simulations *47th Anomalous Absorption Conference.*, Florence, OR

4. **Y. H, Ding**, S. X. Hu, First-principles equation-of-state table of beryllium for High-Energy-Density Plasma Simulations *HEDS Summer School.*, La Jolla, CA

Acknowledgments

I would like to thank my wife and my parents for all your love, support and encouragement during my Ph.D. studies at University of Rochester.

I wish to thank my advisor, Professor John C. Lambropoulos. He has been supportive of me since my day one at department of mechanical engineering of University of Rochester, especially at the most difficult time in these five years PhD experiences. I am deeply grateful for this advice, kindness and generosity without which I could not finish this journey. I express thanks also go to Professor Suxing Hu who provided me with guidance and mentorship at Laboratory for Laser Energetics. He is one of the smartest people I have ever meet. His innovative ideas, immense knowledge and great passion for science always inspire me in my future life. I am grateful to be his student.

My thanks also go to Professor Chuang Ren, Professor Brendan Mort and Professor Pengfei Huo for agreeing to serve on my thesis committee and provide valuable guidance.

Abstract

Warm Dense Matter(WDM) or High Energy Density(HED) plasmas are encountered in many fields of science ranging from planetary science and astrophysics to inertial confinement fusion(ICF). In ICF implosions, the deuterium-tritium fuel and ablator materials undergo various extreme state of matter. Accurately knowing of the properties of material under such conditions is essential to both understand the implosion physics and to design the ICF targets. Quantum molecular-dynamics(QMD), based on Density Functional Theory(DFT), has been successfully applied to investigate the equation of state, thermal and electrical conductivities and optical absorptions of warm dense plasma. However, these QMD studies based on Kohn-Sham DFT cannot access to the HED plasmas with relatively high temperature and low densities. In this Ph.D. project, a time-dependent orbital-free density functional theory (TD-OF-DFT) simulation package has been developed for *ab initio* investigations of charged-particle stopping power of warm dense matter . Our current dependent TD- OF-DFT calculations have reproduced the recently well-characterized stopping power experiment in warm dense

beryllium. For α-particle stopping in warm and solid-density DT plasmas, the ab initio TD-OF-DFT simulations show a lower stopping power up to 25 % in comparison with three stopping-power models often used in the high-energy-density physics community.

Contributors and Funding Sources

This work was supported by a dissertation committee consisting of Professor John Lambropoulos(advisor) and Professor Chuang Ren of the Department of Mechanical Engineering and Professor Brendan Mort and Professor Pengfei Huo of the Department of Chemistry. The analyses depicted in Section 3.5 were conducted by Alexander White in Los Alamos National Laboratory and were published in 2018 in an article listed in the Biographical Sketch. All other work conducted for the dissertation was completed by the student independently. The author was supported by Frank Horton Fellowship from the Laboratory for Laser Energetics.

This work was supported by the U.S. Department of Energy (DOE) National Nuclear Security Administration under Award No.DE-NA0001944, the University of Rochester; and the New York State Energy Research and Development Authority.

List of Figures

Chapter 1

Introduction

1.1 High Energy Density Physics and Warm Dense Matter(WDM)

High Energy Density Physics (HEDP) is the study of matter at extreme conditions. It is a new and promising intersection field of different traditional physical fields including plasma physics, nuclear physics and solid state physics. The study of HEDP is the key to understand and control the extreme matter. Warm Dense Matter(WDM) is encountered in many fields of science ranging from planetary science and astrophysics to inertial confinement fusion(ICF). It is often defined as a region where both strongly coupled and degeneracy effects are important. In this regime, where traditional classical plasma physics assumptions break down, quantum and many-body effects also play an important role. Strong many-body coupling and quantum electron degeneracy effects play essential roles in determining material properties in the WDM regime. In recent years, HEDP and WDM have gained

more attention including astrophysics and inertial confinement fusion. At the same time, WDM is also the state that is hard to model theoretically as quantum degeneracy, Coulomb correlations and thermal effects need to be taken into account. In ICF implosions(Betti and Hurricane, 2016), the deuterium-tritium(Hu et al., 2011) (Hu et al., 2014) fuel and ablator materials (Hu et al., 2015*a*; Hu, Boehly and Collins, 2014) undergo various extreme states of matter. Accurately knowing the properties of material including both static and dynamic under such conditions is essential to both understand the implosion physics and to design the ICF targets (Krauser et al., 1996; Dittrich et al., 1999). Quantum molecular-dynamics(QMD) (Collins et al., 1995) (Clérouin and Bernard, 1997) (Collins et al., 2001), based on Density Functional Theory(DFT), has been successfully applied to investigate the equation of state (Benedict et al., 2014) (Hu et al., 2015*b*), thermal and electrical conductivities and optical absorptions of warm dense plasma. However, these QMD studies based on Kohn-Sham DFT cannot access the HED plasmas with relatively high temperature and low densities. This work will focus on developing Time-Dependent Orbital-Free Density Functional Theory code to study the properties of HED plasmas.

1.2 Equation of State(EOS)

In high energy density physics, the EOS plays an essential role in modeling the overall physical process. For example, in inertial confinement fusion

(ICF) experiments, the EOS is critical in simulating the overall implosion and is an essential piece of ICF experiments design. Static properties such as EOS under extreme conditions can be studied using different first-principles methods, such as DFT-based quantum molecular-dynamics (QMD), path-integral Monte Carlo(PIMC) (Pierleoni et al., 1994), and quantum Monte Carlo (QMC) (Tubman et al., 2015). Theoretical EOS models are particularly difficult to generate in the so-called warm-dense-matter (WDM) regime, where both strongly coupled and degeneracy effects are important (Nellis et al., 1997*b*). In this regime, where traditional classical plasma physics assumptions break down, quantum and many-body effects must be taken into account. Various theoretical models have been developed to predict the EOS of different materials. In this thesis, we will mainly focus on silicon and Beryllium.

Beryllium (Be), which has many applications in nuclear power, electronic, geophysics, and aerospace industries, is an element of great technological and scientific importance for its simple atomic configurations. In inertial confinement applications, beryllium has been used as an ablator for indirect-drive fuel capsule designs (Simakov et al., 2014) because of its advantages of high density, low opacity, high thermal conductivity (Wilson et al., 1998). Since these target designs are based mainly on the radiation–hydrodynamic simulations where the materials will experience many different pressure (up to 105 Mbar) and temperature (up to 108 K) conditions (Nellis et al., 1997*b*), accurate properties of beryllium under such extreme conditions are essential

for ICF applications. Experimental data are limited to 20 Mbar, however, because of the difficulty in generating shocks and measuring them accurately. Hydrodynamic (hydro) simulations require a full equation-of- state (EOS) table to cover all plasma conditions concerned. Therefore, it is of great importance to calculate the EOS of beryllium for a wide range of conditions by using reliable methods. Once the calculated EOS table is benchmarked with experiments, it can be used for reliable ICF and high-energy- density target designs and simulations. Silicon (Si) as one of the most abundant elements on Earth, is also essential to both ICF and geophysics applications since it is needed for hydrodynamic simulations of ICF implosions (used as dopants to ablators in indirect-drive ICF target designs) and for understanding the geophysics of the Earth's outer core. In Chapter 2, the QMD method will be presented in detail. In particular, I will introduce the Orbital-Free DFT method in the section as the preparation for the implementation of time dependent part. Both our FPEOS Hugoniot curve and off-Hugoniot is compared with several theoretical and experimental data. The FPEOS is also implemented into *LILAC* to investigate how the different EOS tables will affect ICF implosions using beryllium as the ablator.

1.3 Electronic Transport Properties

Electronic transport properties of warm dense matter, such as electrical or thermal conductivities and non-adiabatic stopping power, are of particular

interest to geophysics, planetary science, astrophysics, and inertial confinement fusion (ICF). One specific example is the α-particle stopping power of dense deuterium-tritium (DT) plasmas, where an uncertainty of 20 %in stopping power could lead to a 50 % variation in the energy required for ignition. Accurate stopping power is therefore a key component for hydro- dynamic modeling of ICF, astrophysics, and other fusion processes. In this thesis, I will examine both α-particle and proton stopping in various materials under different conditions.

A combination of simplified models, analytical limits, and semiempirical approaches have historically determined the stopping power of materials (Li and Petrasso, 1993*b*) (Brown, Preston and Singleton Jr, 2005*b*) (Singleton Jr, 2008*b*). For low- temperature or high-density systems, first-principles methods based on a quantum mechanical treatment of the electrons provide accurate static, transport, and conductive properties. These methods include finite-temperature density functional theory (DFT)-based quantum molecular dynamics, path-integral Monte Carlo, and quantum Monte Carlo calculations. In particular, the Kohn-Sham (KS) orbital-based DFT method has been extensively used to calculate transport properties for various materials, including both ionic and electronic transport in the time-independent formalism (Desjarlais, 2003) (Recoules et al., 2009). In addition, the Kohn-Sham time-dependent DFT method has recently been applied to x-ray Thompson scattering (XRTS) (Baczewski et al., 2016) and the stopping power of materials well below the Fermi temperatures (TF) (Magyar, Shulenburger and

Baczewski, 2016). For cold condensed matter systems, stopping power can be modeled from first-principles using real-time time-dependent density functional theory (DFT). However, high temperatures (10's to 100's of eV) may be computationally prohibitive for traditional Kohn-Sham DFT. Strong many-body coupling and quantum electron- degeneracy effects play essential roles in determining material properties in the WDM regime (Nellis et al., 1997*b*), which renders the traditional plasma-physics models no longer valid. Ab initio approaches which can treat crossover regimes, without system specific corrections, are thus highly desirable. Unfortunately, like we stated before, extending the Kohn-Sham DFT approach beyond T_F becomes computationally difficult because of the large number of occupied eigenstates required. For example, recent stopping-power experiments (Zylstra et al., 2015) (Frenje et al., 2015) performed with warm dense plasmas ($T > T_F$) present particular difficulties. Despite these and other experiments (Cayzac et al., 2017), as well as theoretical studies (Fu et al., 2016) (Kim et al., 2015*a*) (Kim et al., 2015*b*), a stringent test of stopping-power models with first principles simulations in the WDM regime remains elusive. In this project, we offer a prescription to extend DFT methods for stopping power to high temperatures and densities through a time-dependent orbital-free (OF) formulation. We then compare our results with predictions from three stopping-power models, Li-Petrasso (Li and Petrasso, 1993*a*) (LP), Brown-Preston-Singleton (BPS) (Brown, Preston and Singleton Jr, 2005*a*) (Singleton Jr, 2008*a*), and RPA dielectric function (Singleton Jr, 2008*c*) (DF), for both the Be experiment

and the proposed experiment of α-particle stopping in DT.

Chapter 2

Ab initio studies on static properties of warm dense plasmas

Quantum molecular dynamics (QMD) based on the density-functional theory (DFT), has proven to be a reliable method for studying the many-body quantum systems of dense plasma. QMD simulations have been shown to work well for EOS calculations such as deuterium, CH, silicon carbon,and quartz. The most-recent first- principles calculations, which combined the orbital - based DFT Kohn - Sham molecular dynamics (KSMD) and orbital-free molecular dynamics (OFMD), have established wide-ranged and consistent first-principles EOS (FPEOS) tables for CH and silicon. These studies have also indicated that the observed EOS differences can have significant effects on hydro-simulations. In this Chapter, QMD simulations were used to calculate the Be-EOS table for a wide range of densities ($\rho = 0.001$ g/cm3 $\rho = 500$ g/cm3) and temperatures ($T = 2000$ K to $T = 10^8$ K). From the established FPEOS table, we derived the principal Hugoniot curve using the Rankie–Hugoniot equation and compared our calculations with several

theoretical models and available experimental data. We also studied the pressure and internal energy differences between FPEOS and *SESAME* 2023 for off-Hugoniot conditions. With the implementation of our FPEOS table of beryllium into our radiation–hydrodynamics code *LILAC*, we investigate the EOS effects on ICF simulations. The QMD method is described in Sec 1. Our FPEOS Hugoniot curve is compared with several theoretical and experimental data in Sec 2. The off-Hugoniot comparisons between FPEOS and *SESAME* 2023 are shown in Sec 2. In Sec 3, the FPEOS is implemented into *LILAC* to investigate how the different EOS tables will affect ICF implosions using beryllium as the ablator.

2.1 Quantum molecular dynamic method

In recent years, first-principles method (or *ab initio*), including the DFT based QMD, path-integral Monte Carlo(PIMC), and quantum Monte Carlo (QMC) have made substantial progress in predictig the properties of materials at extreme conditions. QMD, combining the laws of quantum mechanics and classical molecular dynamics, has been proven to be an effective computational approach to treating materials under extreme conditions. Based on the finite-temperature density-functional theory, traditional QMD implementation uses the Kohn - Sham orbitals to represent the many - particle system in terms of single - particle orbitals. The KSMD method is accurate and computationally efficient at temperatures generally below the electron

Fermi temperature $T_F = E_F/k_b = (3\pi^2\rho)^{2/3}/2k_b$, in atomic unit, Fermi vector $k_F = (3\pi^2\rho)^{1/3}$. At high temperature region $T > T_F$ however it becomes impractical because of the increasing number of energy bands needed to represent the thermal-excited electrons $\rho(\mathbf{r}) = \sum_i f_i|\psi_i(\mathbf{r})|^2$ according to Fermi - Dirac distribution $f_i = (1 + e^{(\epsilon_i-\mu)/k_bT})^{-1}$. In contrast, the other QMD implementation is OFMD, which greatly improves the computational efficiency by eliminating orbitals. In the OFMD treatment, the total free energy of a many-particles system is expressed only in terms of electron density according to an improved Thomas–Fermi–Dirac (TFD) model. The computational efficiency at $T > T_F$ is at the expense of precision resulting from the approximation of the TFD model. Nonetheless, the pressure predicted by OFMD differs from the KSMD prediction by only 1% in the vicinity of Fermi temperature where both methods are applicable.

2.1.1 Kohn-Sham density functional theory

The Kohn-Sham scheme imagines a system of N non-interacting electrons that yield the electronic density of the original interacting N electron system. These fictitious electrons sit in a new external potential called the KS potential. The KS scheme is written as a set of equations that must be solved self-consistently :

$$\left\{-\frac{1}{2}\nabla^2 + V_H + V_{ext} + V_{xc}\right\}\phi_i(\mathbf{r}) = \epsilon_i\phi_i(\mathbf{r}) \tag{2.1}$$

$$\rho(\mathbf{r}) = \sum_i f_i |\phi_i(\mathbf{r})|^2 \tag{2.2}$$

$$f_i = (1 + e^{(\epsilon_i - \mu)/k_b T})^{-1} \tag{2.3}$$

where $\phi(\mathbf{r})$ and $\epsilon\mathbf{r}$ are the KS orbitals and energies, μ is chemical potential. $V_H = \int d\mathbf{r} \frac{\rho(\mathbf{r})}{|\mathbf{r} - \mathbf{r}|}$ is classical Hartree potential and $V_{xc} = \frac{\delta E_{xc}}{\delta \rho(\mathbf{r})}$ is exchange-correlation potential defined by the unknown XC energy. These must be solved self-consistently since the Hartree potential and Exchange-Correlation term depend explicitly on the density.

In this project, in order to make the wave function near the core regions smoother, a projector-augmented wave (PAW) pseudopotential was generated to replace the pure Coulomb potential. The electron exchange-correlation potential is modeled by the Perdew–Burke–Ernzerhof (PBE) functional in the generalized-gradient approximation (GGA). The electrons are described by quantum-mechanical wave functions, and the nuclei (ions) are treated as classical particles governed by the Newtonian mechanics.

2.1.2 Orbital-free density functional theory

The OFMD method describes the ground-state energy of a many-particle system as a function of electronic density without constructing Kohn - Sham orbitals. The main feature that distinguishes the OFMD from the KSMD is the expression for the kinetic - energy term. In the OFMD approach, the

kinetic energy is derived using the TFD model at a finite temperature plus the von Weizsäcker correction taking into account the gradient correction of the density. The finite temperature Thomas Fermi term is related to electron density through following equations :

$$\begin{aligned}
\frac{A}{V} &= -\frac{2}{3}(\frac{m}{\hbar^2})^{3/2}\frac{\sqrt{2}}{\pi^2\beta^{5/2}}\int\frac{x^{3/2}}{z^{-1}e^x+1}dx+\mu\frac{N}{V} \\
&= -\frac{2}{3}(\frac{m}{\hbar^2})^{3/2}\frac{\sqrt{2}}{\pi^2\beta^{5/2}}\int\frac{x^{3/2}}{z^{-1}e^x+1}dx+\mu*(\frac{m}{\hbar^2})^{3/2}\frac{\sqrt{2}}{\pi^2\beta^{3/2}}\int\frac{x^{1/2}}{z^{-1}e^x+1}dx \\
&= -\frac{2}{3}(\frac{m}{\hbar^2})^{3/2}\frac{\sqrt{2}}{\pi^2\beta^{5/2}}I_{3/2}+\mu*(\frac{m}{\hbar^2})^{3/2}\frac{\sqrt{2}}{\pi^2\beta^{3/2}}I_{1/2} \\
&= -\frac{2}{3}(\frac{m}{\hbar^2})^{3/2}\frac{\sqrt{2}}{\pi^2\beta^{5/2}}I_{3/2}+\beta\mu*(\frac{m}{\hbar^2})^{3/2}\frac{\sqrt{2}}{\pi^2\beta^{5/2}}I_{1/2} \\
&= (\frac{m}{\hbar^2})^{3/2}\frac{\sqrt{2}}{\pi^2\beta^{5/2}}(-\frac{2}{3}I_{3/2}+\beta\mu I_{1/2})
\end{aligned} \tag{2.4}$$

$$\begin{aligned}
\frac{N}{V} &= (\frac{m}{\hbar^2})^{3/2}\frac{\sqrt{2}}{\pi^2\beta^{3/2}}\int\frac{x^{1/2}}{z^{-1}e^x+1}dx \\
&= (\frac{m}{\hbar^2})^{3/2}\frac{\sqrt{2}}{\pi^2\beta^{3/2}}I_{1/2}
\end{aligned} \tag{2.5}$$

Where A is the free energy of the system, V is the volumn of the system, N is the number of particles in the system. $z = e^{\mu/k_bT}$ is fugacity $\beta = 1/(k_bT)$.

And Fermi Integral $I_{1/2}$is defined as :

$$I_{1/2} = \int \frac{x^{1/2}}{z^{-1}e^x + 1} dx \tag{2.6}$$

The von Weizsäcker correction is written as $F_{vw} = \int h(\rho(\mathbf{r})) \frac{|\nabla \rho(\mathbf{r})|^2}{\rho(\mathbf{r})} dr$. The $h(\rho(\mathbf{r}))$ is an analytical corrrection term given by F. PerrotPerrot (1979) to generalize the term int to finite temperatures. After introdcue these two terms represent the kinetic energy and minimize the free energy of the system with respect to the density, we got a nonlinear Schrödinger like equation $H(\rho(\mathbf{r}))\psi(\rho(\mathbf{r})) = \mu\psi(\rho(\mathbf{r}))$ where

$$H(\rho(\mathbf{r})) = -\frac{1}{2}\nabla^2 + [\frac{\delta F_{TF}}{\delta \rho(\mathbf{r})} + \frac{\delta F_{xc}}{\delta \rho(\mathbf{r})} + V_{ext} + \int d\mathbf{r} \frac{\rho(\mathbf{r})}{|\mathbf{r} - \mathbf{r}|}] \tag{2.7}$$

In this case, the electron density is expressed the sum a "collective orbital" $\rho(\mathbf{r}) = |\psi(\mathbf{r})|^2$. Note that the introduction of the single "orbital" rather than density is for numerical convenience. Using the normalization constraint $\int |\psi(\mathbf{r})|^2 d\mathbf{r}$ for N total electrons. The F_{TF} term the Thomas-Fermi (TF) kinetic-energy functional. The Laplacian operator arises from the minimization of the von Weizsäcker term. The Exchange Correlation term, external potential and Hartree term is same as KS formalism.

In OFMD simulations, we assume that the beryllium plasmas are in the local thermodynamic equilibrium (LTE); Relativistic effects in our simulation region are negligible; and bound states and continuum states are treated

in the same way. The exchange-correlation functional is expressed in the local density approximation of Perdew and Zunger. The time evolution of the system was also calculated in two steps. The electrons were treated quantum mechanically and ions were classical particles. The difference here is that we minimized the electron-free energy with respect to the electron density directly, rather than minimizing with respect to the orbitals in the KSMD case.

2.2 First-principles equation-of-state(FPEOS) table of Beryllium

Combining the calculations of KSMD and OFMD, we examined the widely ranged beryllium conditions in the pressure–temperature ($P-T$) space. The pressure and internal energy were obtained for all the sampled density and temperature points ($\rho = 0.001$ g/cm3 $\rho = 500$ g/cm3) and temperatures ($T = 2000$ K to $T = 10^8$ K). We make the transition from KSMD to OFMD at the temperature point $T = 250000K$, where their differences are within $\sim 1\%$. The total pressures as a function of the beryllium temperature are shown in Fig. 2.1.

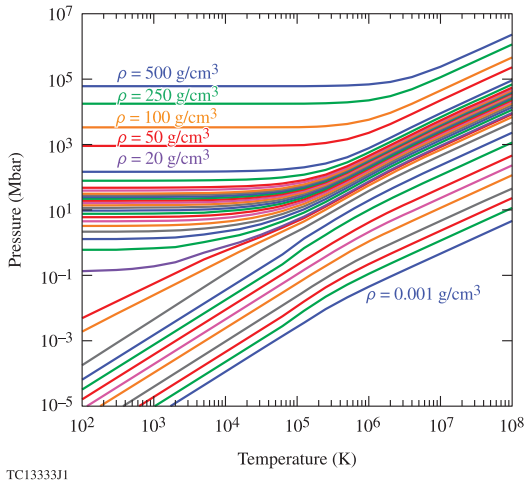

Figure 2.1: The pressure as a function of beryllium plasma temperature for all densities ($\rho = 0.001$ to 500 g/cm3) by our first-principle Kohn-Sham and orbital-free molecular dynamics calculations.

2.2.1 Principle Hugoniot conditions comparison

The shock Hugoniot curve can be derived from the resulted FPEOS table according to the Rankine - Hugoniot equation

$$\text{Hug} = E_f - E0 + \frac{1}{2}(P_f + P_0)(\frac{1}{\rho_f} + \frac{1}{\rho_0}) \tag{2.8}$$

where the initial pressure, internal energy, and density of the beryllium before the shock are represented by (P_0, E_0, q_0) and the quantities after shock are given by (P_f, E_f, q_f).

To compute the princi- pal Hugoniot, we chose the initial state to be the solid beryllium, (ρ =1.84g/cm3) at ambient temperature (T = 300K). Substituting the EOS data into the Hugoniot equation, we can derive the principal Hugoniot of Be. *SESAME* EOS was constructed using various combinations of different theoretical models and constrained by best-avaiable experiment data in different regions.

Fig.2.2 shows that the FPEOS Hugoniot pressure of beryllium is in good agreement (within 10%) with the widely used *SESAME* model (*SESAME* 2023) in the low- compression-ratio region ($\rho/\rho_0 < 3$); however, the pressure differences can be up to 30 % in the high compression region. Fig.2.2 also shows that the peak compression ratio decreases slightly from 4.33 (FPEOS calculation) to 4.26 (*SESAME* prediction), which indicates that under shock compression, beryllium is slightly softer than the SESAME model near the maximum compression. This is mainly because the the model overestimates

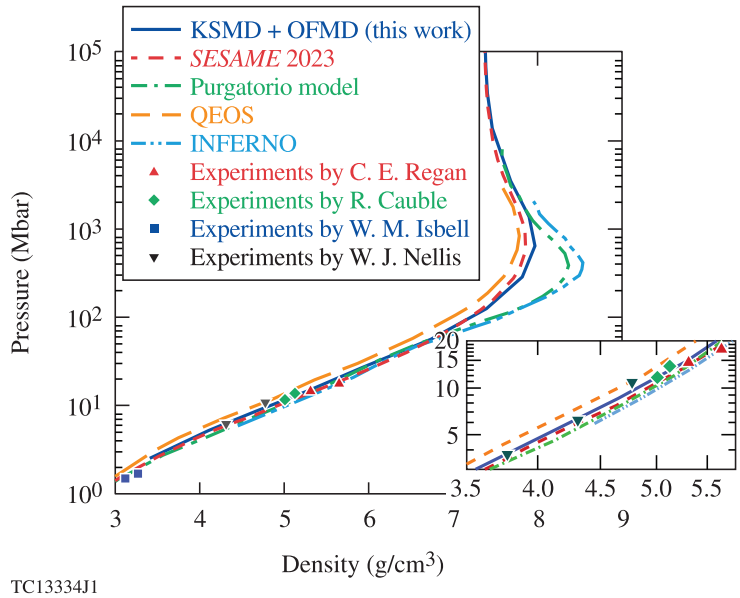

Figure 2.2: The Rankine–Hugoniot curve of beryllium predicted by the first-principles equation of state (FPEOS) (solid blue line) is compared with the *SESAME* 2023 model (dashed red line), the Purgatorio modelWilson et al. (2006) (dotted– dashed green line), the QEOS modelMore et al. (1988) (dashed orange line), the INFERNO model Liberman and Bennett (1990) (dotted–dashed blue line), and available experiments (various symbols) by Regan,Ragan (1982) Cauble et al.,Cauble et al. (1998) Isbell et al., and Nellis et al.Nellis et al. (1997*a*)

the ionization of electrons, leading to too-large a pressure along the Hugoniot curve for the same shock density. As the shock pressure continues to increase, the density predicted by both the FPEOS and SESAME reaches an ideal gas limit ($\rho/\rho_0 = 4$). Experimental data for beryllium have also been plotted in Fig. 2.2 for comparison. Most of models seemed to agree well with the available experimental data. To the best of our knowledge, no published experiments data have been found above 20 Mbar. Future experimental data are needed to benchmark the theoretical models in the pressure region ranging from 50 Mbar to 500 Mbar.

2.2.2 Off-Hugoniot conditions comparison

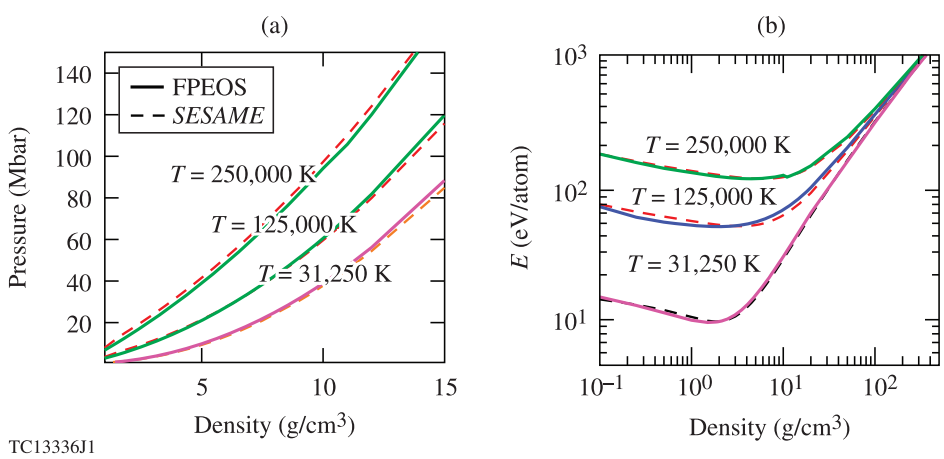

Figure 2.3: The off-Hugoniot equation of state (EOS) isothermal comparisons between FPEOS and SESAME 2023. The (a) pressure and (b) internal energy are plotted as functions of the beryllium density for T = 31,250 K, T = 125,000 K, and T = 250,000K.

Next, we compare the pressure and internal energy of beryllium plasma

for off-Hugoniot plasma conditions between FPEOS and *SESAME* prediction 2023 in Fig.2.3. Fig.2.3(a) shows the pressure as a function of density of beryllium at $T = 31,250$K, $T = 125{,}000$ K, and $T = 250{,}000$K, while the internal energy comparisons are plotted in Fig.2.3(b) which indicates that the internal energy per atom reaches minimum at density ~ 2.5g/cm^3 for $T = 31{,}250$K. This internal energy minimum, manifesting the maximum electronic–ion interaction, increases with temperature, and the corresponding density having minimum internal energy also increases with temperature.

2.3 EOS effects on beryllium-shell-target implosions

Implementing the FPEOS table of beryllium into our radiation–hydrodynamics code *LILAC*, we can examine the EOS effects on HED plasma simulations. The range of the extrapolated EOS table is wide enough for LILAC simulations. Since plasmas generally undergo several regimes including both strongly coupled and degenerate regions during the ICF implosion, an integrated ICF implosion can be used to study the EOS effects. In this section, we simulate a National Ignition Facility (NIF) - type direct-drive implosion.

Fig. 2.4 shows the step laser pulse and dimensions of the target. The duration of the laser pulse is 10 ns with a total energy of 1.5 MJ. The capsule of the simulation had a 80 μm Be layer filled with deuterium-tritium (DT) gas. We launched two simulations: one used beryllium FPEOS and the other

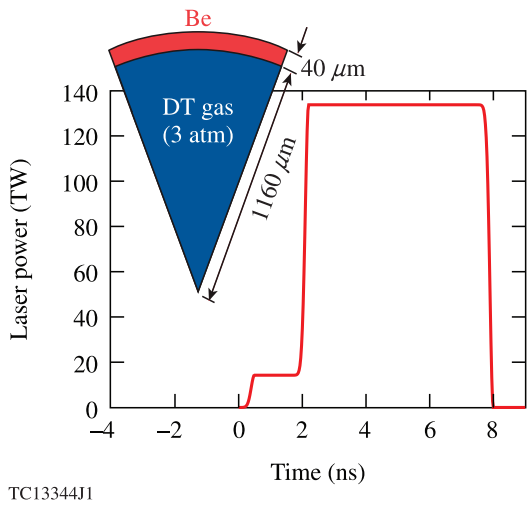

Figure 2.4: The dimensions of the target (inset) and the laser pulse shape for implosion simulations to study how EOS differences will affect hydro simulations. The capsule was made of a 80 μm Be layer filled with 1420 μm of deuterium - tritium (DT) gas. The duration of the step laser pulse was 10 ns with a total energy of 1.5 MJ.

used the $SESAME$ 2023. For the DT gas the two simulations used the same FPEOS. Once the lasers were launched, the Be layer was ablated, which resulted in a shock propagating into the shell. Fig. 2.5 shows a snapshot of the density and temperature profiles at t =2.2 μs versus the target radius for two simulations. At this time, the first shock front was located at $R \sim 1446$ μm with the main shock front behind it which indicates that the shock was still propagating inside the Be layer. We can see that the FPEOS simulation predicts a slightly lower density $\sim 2\%$ than $SESAME$ 2023 since FPEOS is slightly stiffer than $SESAME$ EOS in the temperature region. The shock location in the FPEOS simulation is almost the same as in the $SESAME$ case. The reason behind this phenomenon is that shock speed depends on

the shock density through the formula $V_s = \sqrt{P_s/\rho_0}\,\sqrt{1-\rho_0/\rho_s}$, from which we obtain a very small differences. In addition, the hydro simulation with FPEOS predicts an ~ 4 % lower temperature than the $SESAME$ case.

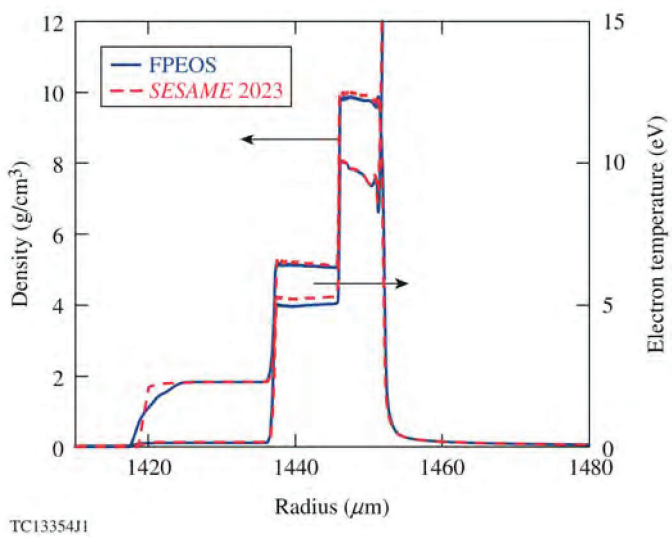

Figure 2.5: The density and temperature profile comparisons between the FPEOS (solid blue line) simulation and $SESAME$ 2023 (dashed red line) simulation. At time $t = 2.2$ns, the shock front is located at $R \sim 1446$ μm, which indicates that the shock is still propagating inside the Be layer.

We also took a snapshot $t = 10$ ns, where the shell was at the end of the acceleration and plotted both the density profile and the electron temperature profile as functions of the target radius. One sees from Fig. 2.6 (a) that the peak density predicted by the FPEOS is 3% lower than predicted by $SESAME$ simulations. The temperature at peak density predicted by FPEOS was $\sim$ 16.6 eV, while the SESAME prediction was $\sim$ 15.7 eV, a difference of $\sim$ 6%. We can see that at the back surface of the shell, there are

more significant temperature differences ($\sim$ 18%). Fig. 2.6(b) plots density and ion temperature as functions of radius at the peak compression (t = 12 ns). In these situations, the differences between FPEOS and SESAME simulations are small even for peak density as with the temperature increase above $T > 10^6$ K.

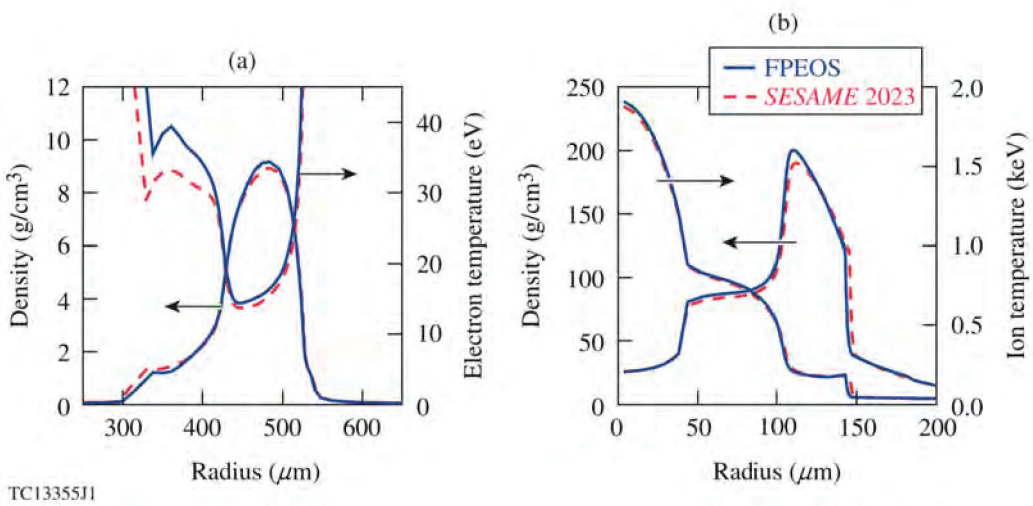

Figure 2.6: Same as Fig.2.5 but for different implosion time : (a) t = 10 ns where the shell is at the end of acceleration and (b) = 12 ns where it is at peak compression.

Finally, we compared the overall target performance between the FPEOS and $SESAME$ simulations. The FPEOS simulation also predicted a higher total neutron yield $Y = 3.76 \times 10^4$, which is $\sim$ 15 % higher than $SESAME$ simulation.

Chapter 3

TD-OF-DFT Simulation Package Development

3.1 Orbital-Free DFT foundations

In this section, we calculate the potential in Fourier space. We calculated the potential energy and the derivative of the potential, which will be used in following minimize process. The function Free Energy Or Derivative will do one of two jobs.

In periodic boundary conditions, the Fourier transform can be written as:

$$\begin{aligned} V(\mathbf{r}) &= \sum_{G} V(\mathbf{G}) e^{-i\mathbf{G}\cdot\mathbf{r}} \\ V(\mathbf{G}) &= \frac{1}{\Omega} \int V(\mathbf{r})) e^{i\mathbf{G}\cdot\mathbf{r}} d\mathbf{r} \end{aligned} \tag{3.1}$$

When come to discreet pay attention to the differences of summation and integration, integration includes the summation and the small volume ele-

ments.

$$\begin{aligned} \sum_{x=a}^{b} f(x)\delta x &= \int_a^b f(x)dx \\ \sum_G &= \frac{\int d\mathbf{r}}{dV} = \frac{\int d\mathbf{r}}{(2\pi/L)^3} \end{aligned} \tag{3.2}$$

In the periodic box, the **Delta function** should normalized as :

$$\frac{1}{V}\int_{box} d^3\mathbf{r} e^{i(\mathbf{k}-\mathbf{k}')} = \delta_{\mathbf{k},\mathbf{k}'} \tag{3.3}$$

After Fourier transform:

3.1.1 Hartree terms in planewaves

According to Poisson's equation:

$$\nabla^2 V(\mathbf{r}) = -4\pi n(\mathbf{r}) \tag{3.4}$$

After Fourier transform:

$$G^2 V(G) = 4\pi n(G) \tag{3.5}$$

The Fourier component of electron-electron interaction energy is as following. I think this terms is a non-local potential, which is not confined by the single box. Pay attention, here is the potential density. True potential

$$V_{ee}(G) = \frac{4\pi n(G)}{G^2} \tag{3.6}$$

where

$$n(r) = \sum_G n(\mathbf{G}) e^{-i\mathbf{G}\cdot\mathbf{r}} \tag{3.7}$$

The Fourier representation of the Hartree energy term is, since the integration is done in the single box, this energy should be the energy of the box, not the whole space.

$$\begin{aligned} \frac{1}{2}\int\int d\mathbf{r}d\mathbf{r'}\frac{n(\mathbf{r})n(\mathbf{r'})}{|\mathbf{r}-\mathbf{r'}|} &= \frac{1}{2}\Omega_{cell}\sum_G V_{ee}(\mathbf{G})n^*(\mathbf{G}) \\ &= 2\pi\Omega_{cell}\sum_G \frac{n^2(\mathbf{G})}{G^2} \end{aligned} \tag{3.8}$$

Pay attention how to use Hartree potential energy in the minimization. This term is calculated in the function "free energy or derivative" using what we derived for Hartree potential. And then, using Parseval's theorem to calculate the energy. However, when do the minimization of the energy, we minimize with respect to the density, the result after that might only be the potential.

The following integral in Fourier space transform the potential into the potential energy. Considering the complex conjugate, the product becomes the sum of both Re part and Im part. We can do this because the potential

energy is a real number. This calculating is in ElectronicFunctionals. In The Adiabatic Approximation we do it again, use the conjg directly. They are the same.

$$\begin{aligned}\int d\mathbf{r} n(\mathbf{r}) V_{ee}(\mathbf{r}) &= \Omega \sum_{\mathbf{G}} n(\mathbf{G}) V_{ee}^{*}(\mathbf{G}) \\ &= \Omega \sum_{\mathbf{G}} (Re(n(\mathbf{G}))Re(V_{ee})(\mathbf{G})) + Im(n(\mathbf{G}))Im(V_{ee})(\mathbf{G})))\end{aligned} \tag{3.9}$$

The Coulomb's potential induced by the electron density could be written in atomic unit as:

$$
\begin{aligned}
V(\mathbf{r}) &= \int_{allspace} \frac{n(\mathbf{r}')}{|\mathbf{r}-\mathbf{r}'|} d\mathbf{r}' \\
&= \int_{allspace} \frac{\sum_{\mathbf{G}} n(\mathbf{G}) e^{-i\mathbf{G}\cdot\mathbf{r}'}}{|\mathbf{r}-\mathbf{r}'|} d\mathbf{r}' \\
&= \sum_{\mathbf{G}} \int_{allspace} \frac{n(\mathbf{G}) e^{-i\mathbf{G}\cdot\mathbf{r}'}}{|\mathbf{r}-\mathbf{r}'|} d\mathbf{r}' \\
&= \sum_{\mathbf{G}} \int_{allspace} \frac{n(\mathbf{G}) e^{i\mathbf{G}\cdot\mathbf{u}}}{|\mathbf{u}|} d\mathbf{u} \\
&= \sum_{\mathbf{G}} e^{-i\mathbf{G}\cdot\mathbf{r}} \int_{allspace} \frac{n(\mathbf{G}) e^{-i\mathbf{G}\cdot(\mathbf{r}-\mathbf{u})}}{|\mathbf{u}|} d\mathbf{u} \\
&= \sum_{\mathbf{G}} e^{-i\mathbf{G}\cdot\mathbf{r}} \int_{allspace} \frac{n(\mathbf{G}) e^{i\mathbf{G}\cdot\mathbf{u}}}{|\mathbf{u}|} d\mathbf{u} \\
&= \sum_{\mathbf{G}} e^{-i\mathbf{G}\cdot\mathbf{r}} n(\mathbf{G}) \int_0^{2\pi} d\phi \int_0^{\pi} e^{iGucos\theta} sin\theta d\theta \int_0^{+\infty} udr \\
&= 2\pi \sum_{\mathbf{G}} e^{-i\mathbf{G}\cdot\mathbf{r}} n(\mathbf{G}) d\theta \int_0^{+\infty} \frac{e^{iGu} - e^{-iGu}}{iG} dr \\
&= 4\pi \sum_{\mathbf{G}} e^{-i\mathbf{G}\cdot\mathbf{r}} n(\mathbf{G}) d\theta \int_0^{+\infty} \frac{sin(Gu)}{G} dr \\
&= 4\pi \sum_{\mathbf{G}} \frac{n(\mathbf{G})}{G^2} e^{-i\mathbf{G}\cdot\mathbf{r}} (1+C)
\end{aligned}
\tag{3.10}
$$

C is a constant. From this expression of $V(r)$, we can get the Fourier component, which is in the same formation as we derived from the poisson's equation. There is a connection between the Coulomb potential and poisson's equation both in real space and fourier space.

$$
\begin{aligned}
\nabla^2 V(\mathbf{r}) &= \nabla^2 \int_{allspace} -\frac{n(\mathbf{r}')}{|\mathbf{r}-\mathbf{r}'|} d\mathbf{r}' \\
&= \int_{allspace} \nabla^2 - \frac{n(\mathbf{r}')}{|\mathbf{r}-\mathbf{r}'|} d\mathbf{r}' \\
&= -\int_{allspace} 4\pi\delta(\mathbf{r}-\mathbf{r}')n(\mathbf{r}')d\mathbf{r}' \\
&= -4\pi n(\mathbf{r})
\end{aligned}
\tag{3.11}
$$

The third step of derivation see quantum homework 4.

3.1.2 The electron ion potential, structure factor, form factor

The ionic potential (the external potential) can be written as following: Now we choose one nuclei and calculating the potential that all the electrons acting on them. If we want to calculate the potential of 128 atoms in the box, we can simply do the summation. τ_j is a vector but i cannot make it bold!

In addition, we want to find the potential at certain position $\mathbf{r}$, τ is the vector from the position to the ion. We also take into account the periodic boundary conditions, at $\mathbf{r} - \tau_j - n\mathbf{L}$ there are also image atoms that contributes to the potential. We sum them together. Change the variable of the integral and use the properties of G, the integral limit will also change when we change the integral variable. In this case, the integral limit will go to the any periodic boxes. So we can change the integral to all the space. The potential we get here should also be the one taking into account all the

space ions.

$$V_{ne}(\mathbf{r}) = \sum_{j=1}^{128} \sum_{nL} V(\mathbf{r} - \tau_j - n\mathbf{L}) \tag{3.12}$$

$$\begin{aligned} V_{ne}(\mathbf{G}) &= \frac{1}{\Omega} \int_{\Omega} d\mathbf{r} \sum_{j=1}^{128} \sum_{nL} V(\mathbf{r} - \tau_j - n\mathbf{L}) e^{i\mathbf{G}\cdot\mathbf{r}} \\ &= \frac{1}{\Omega} \int_{allspace} d\mathbf{r} \sum_{j=1}^{128} V(\mathbf{r} - \tau_j) e^{i\mathbf{G}\cdot\mathbf{r}} \\ &= \frac{1}{\Omega} \int_{allspace} d\mathbf{r} V(\mathbf{r}) e^{i\mathbf{G}\cdot\mathbf{r}} \sum_{j=1}^{128} e^{i\mathbf{G}\cdot\tau_j} \\ &= V_{ne}(\mathbf{G}) \sum_{j=1}^{128} S(\mathbf{G}) \end{aligned} \tag{3.13}$$

Attention should be paied here the structure factor in the code is different from what we derived here, it has $\frac{1}{\Omega}$ in the expression! Once this problem was solve, we can conclude that the Fourier transform of Vie is done over all the space. Like the following the derivation.

where $V_{ne}(\mathbf{G})$ is the single nuclei Fourier component of ionic potential, $S(\mathbf{G})$ is the structure factor, $V_{ne,single}(\mathbf{G})$ is the form factor.

$$V_{ne,single}(\mathbf{G}) = \frac{1}{\Omega} \int_{allspace} d\mathbf{r} V_{ne}(\mathbf{r}) e^{i\mathbf{G}\cdot\mathbf{r}} \tag{3.14}$$

$$S(\mathbf{G}) = e^{i\mathbf{G}\cdot\tau_j} \tag{3.15}$$

The Fourier representation of the ionic energy is as following. In the derivation, the Parseval's theorem was used, which introducing the complex conjugate term. Since the potential is real, its complex conjugate is itself.

$$\begin{aligned}\int d\mathbf{r} n(\mathbf{r}) V_{ne}(\mathbf{r}) &= \Omega \sum_{\mathbf{G}} n(\mathbf{G}) V_{ne}^{*}(\mathbf{G}) \\ &= \Omega \sum_{\mathbf{G}} n(\mathbf{G}) V_{ne,single}(\mathbf{G}) S^{*}(\mathbf{G})\end{aligned} \tag{3.16}$$

First, let us derive the convolution theory in periodic boundary condition: (1D), it is similar in 3D expect the length go to volume.

$$f * g = \int_{box} f(u) g(r-u) du \tag{3.17}$$

then the Fourier transform of this convolution is given by:

$$\begin{aligned}\mathcal{F}[f(r) * g(r)] &= \frac{1}{\Omega} \int_{box} e^{iGr} (\int_{box} f(u) g(r-u) du) dr \\ &= \Omega (\frac{1}{\Omega} \int_{box} e^{iG\tau} g(\tau) d\tau) (\frac{1}{\Omega} \int_{box} e^{iGu} f(u) du) \\ &= \Omega \mathcal{F}[f(r)] \mathcal{F}[g(r)]\end{aligned} \tag{3.18}$$

In the second step we change the variable $\tau = r - u$, finally we found the Fourier transform of convolution is the multiply of Fourier component and

multiply the volume Ω. The volume is the major difference from the standard Fourier transformation. Next, we will use this theory to prove the Fourier transform of ion-electron potential.

$$
\begin{aligned}
&\mathcal{F}[\sum_n V(\mathbf{r}-\tau_j-n\mathbf{L})] \\
=&\mathcal{F}[\int_{box}\sum_n V(\mathbf{x}-n\mathbf{L})\delta(\mathbf{x}-\mathbf{r}+\tau_j)d\mathbf{x}] \\
=&\mathcal{F}[\sum_n V(\mathbf{r}-n\mathbf{L})]\mathcal{F}[\delta(\mathbf{x}-\mathbf{r}+\tau_j)]\Omega \\
=&(\frac{1}{\Omega}\int_{box} V(\mathbf{r}-n\mathbf{L})e^{i\mathbf{G}\cdot\mathbf{r}}d\mathbf{r})(\frac{1}{\Omega}\int_{box} e^{i\mathbf{G}\cdot(\mathbf{x}-\mathbf{r})}d\mathbf{r}\delta(\mathbf{x}-\mathbf{r}+\tau_j))\Omega \\
=&\Omega(\frac{1}{\Omega}\int_{allspance} V(\mathbf{r})e^{i\mathbf{G}\cdot\mathbf{r}}d\mathbf{r})(\frac{1}{\Omega}e^{i\mathbf{G}\cdot\tau_j})
\end{aligned}
\tag{3.19}
$$

3.1.3 The Proof of Parseval's theory in PBC

The result in 1D case is :

$$
\int_{box} f(r)g(r)^* dr = \frac{1}{L}\sum_G f(G)g(G)^* \tag{3.20}
$$

We can write LHS of above equation as:

$$
\int_{box} f(r)g(r)^* dr = \int_{box} (\sum_G f(G)e^{iGr})(\sum_{G'} g^*(G')e^{iG'r})dr \tag{3.21}
$$

Rearrange the order to integration we obtain the theory in periodic boundary condition case.

$$\begin{aligned}\int_{box} f(r)g(r)^* dr &= \sum_G \sum_{G'} f(G)g^*(G')(\int_{box} e^{i(G-G')r} dr) \\ &= \sum_G \sum_{G'} f(G)g^*(G')(L\delta(G,G')) \\ &= L\sum_G f(G)g^*(G)\end{aligned} \tag{3.22}$$

3.1.4 Hellmann Feynman theory

Once we calculated the ironic energy, we can use Hellmann Feynman theory to calculate the force that electrons acting on ions. The theory says:

$$\mathbf{F}_j = -\frac{d}{d\tau_j} \langle \Psi | \hat{H}_{ne} | \Psi \rangle \tag{3.23}$$

If the wave function do not depend on the position of ions, we can take the derivative with respect to the Hamiltonian. In the last step of the derivation, the force should be a real number, so we only take the real part. Finally, we derive the exact form of the force we have in the code.

$$
\begin{aligned}
\mathbf{F}_j &= -\langle\Psi|\frac{d}{d\tau_j}\hat{H_{ne}}|\Psi\rangle \\
&= \frac{d}{d\tau_j}(\Omega\sum_{\mathbf{G}} n(\mathbf{G})V_{ne,single}(\mathbf{G})e^{-i\mathbf{G}\cdot\tau_j}) \\
&= -i\mathbf{G}\Omega\sum_{\mathbf{G}} n(\mathbf{G})V_{ne,single}(\mathbf{G})e^{-i\mathbf{G}\cdot\tau_j} \\
&= \mathbf{G}\Omega\sum_{\mathbf{G}} V_{ne,single}(\mathbf{G})Im((\mathbf{G})e^{-i\mathbf{G}\cdot\tau_j})
\end{aligned}
\tag{3.24}
$$

The potential energy (Vie Vee) is summed over a single box. While the potential is due to the charges all over the space. When we calculate the force, the force is summed over all the space.

3.1.5 Regularized Potentials

This subroutine reads the cut off radius, energy corrections and Regularized Potential from OFMD.input and calculate the Fourier transform of the potential as following:

$$
\begin{aligned}
V(\mathbf{G}) &= \frac{1}{\Omega}\int_{box} V(\mathbf{r})e^{i\mathbf{k}\cdot\mathbf{r}}d\mathbf{r} \\
&= \int_0^{2\pi} d\phi \int_0^{\pi} sin\theta d\theta \int_0^{+\infty} V(r)r^2 e^{ikrcos\theta}dr \\
&= \frac{1}{\Omega}2\pi \int_0^{\pi} sin\theta e^{ikrcos\theta}d\theta \int_0^{+\infty} V(r)r^2 dr \\
&= \frac{1}{\Omega}2\pi \int_0^{+\infty} V(r)r^2 dr \int_0^{\pi} sin\theta e^{ikrcos\theta}d\theta \\
&= \frac{1}{\Omega}2\pi \int_0^{+\infty} V(r)r^2 \frac{e^{ikr}-e^{-ikr}}{ikr}dr \\
&= \frac{4\pi}{\Omega k}\int_0^{+\infty} V(r)rsin(kr)dr \\
&= \frac{4\pi}{\Omega k}(\int_0^{Rc} Vps(r)rsin(kr)dr + \int_{Rc}^{+\infty} sin(kr)dr) \\
&= \frac{4\pi}{\Omega k}[(Rc)^2\int_0^1 Vps(r)rsin(k*Rc*r)dr + \frac{1}{k}(cos(k*Rc)+C)]
\end{aligned}
\tag{3.25}
$$

In the last step of derivation, the use the constant C to represent the upper limit of the integration. In the potential, the constant does not matter, the potential is relative.

$$
\frac{dV(G)}{dG^2} = \frac{1}{2G}\frac{dV(G)}{dG} = \frac{1}{2G}\frac{1}{G}(\frac{d(GV(G))}{dG} - V(G)) \tag{3.26}
$$

where we change the vector into the magnitude of vector.Error function and complimentary error function :

$$erf(x) = \frac{2}{\sqrt{\pi}} \int_0^x e^{-t^2} dt \tag{3.27}$$

$$\begin{aligned} erfc(x) &= 1 - erf(x) \\ &= 1 - \frac{2}{\sqrt{\pi}} \int_0^x e^{-t^2} dt = \frac{2}{\sqrt{\pi}} \int_x^\infty e^{-t^2} dt \end{aligned} \tag{3.28}$$

Next, the definition of short range and long range force. If potential drops down to zero faster than r^{-d}, where r is the separation between two particles and d is the dimension of the problem, it is called short ranged, otherwise it is long ranged.

In the code, we do the Ewald summation to calculate the E-field or potential generated by the nucleus. They are not continuous as the electron density, which we have explored in the Hartree part. The charge density for point charge q_i is

$$n_i(\mathbf{r}) = q_i \delta(\mathbf{r} - \mathbf{r}_i) \tag{3.29}$$

we can split it into two terms by adding and subtracting a Gaussian distribution:

$$n_i^S(\mathbf{r}) = q_i \delta(\mathbf{r} - \mathbf{r}_i) - q_i G(\mathbf{r} - \mathbf{r}_i) \tag{3.30}$$

$$n_i^L(\mathbf{r}) = q_i G(\mathbf{r} - \mathbf{r}_i) \tag{3.31}$$

where

$$\begin{aligned} G(\mathbf{r} - \mathbf{r}_i) &= \frac{1}{(2\pi\sigma^2)^{3/2}} \exp[-\frac{(\mathbf{r} - \mathbf{r}_i)^2}{2\sigma^2}] \\ &= (\frac{\alpha^2}{\pi})^{3/2} \exp[-\alpha^2 (\mathbf{r} - \mathbf{r}_i)^2] \end{aligned} \tag{3.32}$$

where $\alpha = 1/(\sqrt{2}\sigma)$.$\sigma$ is the standard deviation of Gaussian distribution. If the stand deviation is large enough, Gaussian distribution turns into delta function. The potential field then also in two term:

$$V_i^S(\mathbf{r}) = \frac{q_i}{4\pi\varepsilon_0} \int \frac{\delta(\mathbf{r} - \mathbf{r\prime}) - G(\mathbf{r} - \mathbf{r\prime})}{|\mathbf{r} - \mathbf{r\prime}|} d^3\mathbf{r} \tag{3.33}$$

$$V_i^L(\mathbf{r}) = \frac{q_i}{4\pi\varepsilon_0} \int \frac{G(\mathbf{r} - \mathbf{r\prime})}{|\mathbf{r} - \mathbf{r\prime}|} d^3\mathbf{r} \tag{3.34}$$

The potential field generate by charge distribution of the Gaussian can be obtained by solving the Poisson's equation:

$$\nabla^2 V(\mathbf{r}) = -\frac{qG(\mathbf{r})}{\varepsilon_0} \tag{3.35}$$

Since the Gaussian in 3D is also symmetry, only depend on the magnitude r. We try to solve the Poisson's equation in spherical coordinates:

$$\begin{aligned}
\frac{1}{r}\frac{\partial^2}{\partial r^2}[rV(r)] &= -\frac{qG(r)}{\varepsilon_0} \\
\frac{\partial}{\partial r}[rV(r)] &= q\int -\frac{rG(r)}{\varepsilon_0}dr = \frac{\sigma^2}{\varepsilon_0}qG(r) \\
rV(r) &= \frac{\sigma^2}{\varepsilon_0}q\int_0^r G(r)dr = \frac{\sigma^2}{\varepsilon_0}\frac{q}{(2\pi\sigma^2)^{3/2}}\sqrt{\frac{\pi}{2}}erf(\frac{r}{\sqrt{2}\sigma}) \\
V(r) &= \frac{q}{4\pi\varepsilon_0 r}erf(\frac{r}{\sqrt{2}\sigma})
\end{aligned} \tag{3.36}$$

where $erf(x) = \frac{2}{\sqrt{\pi}}\int_0^x e^{-t^2}dt$. Therefore:

$$V^S(\mathbf{r}) = \frac{q}{4\pi\varepsilon_0|\mathbf{r}-\mathbf{r}_i|}\text{erfc}(\frac{|\mathbf{r}-\mathbf{r}_i|}{\sqrt{2}\sigma}) \tag{3.37}$$

$$V^L(\mathbf{r}) = \frac{q}{4\pi\varepsilon_0|\mathbf{r}-\mathbf{r}_i|}\text{erf}(\frac{|\mathbf{r}-\mathbf{r}_i|}{\sqrt{2}\sigma}) \tag{3.38}$$

Because $\lim_{z\to\infty}\text{erf}(z) = 1$,we can see that V^S is the short range potential, we distance is large, the potential is weak. $V^L(\mathbf{r})$ is the long range potential, when distance is large, the potential is large. Considering the periodic boundary conditions, the short range potential and potential energy can be written as:

$$V^S(\mathbf{r}) = \frac{1}{4\pi\varepsilon_0}\sum_{\mathbf{n}}\sum_{j=1}^{N}\frac{q_j}{|\mathbf{r}-\mathbf{r}_i+\mathbf{n}L|}\text{erfc}(\frac{|\mathbf{r}-\mathbf{r}_i+\mathbf{n}L|}{\sqrt{2}\sigma}) \tag{3.39}$$

$$E^S(\mathbf{r}) = \frac{1}{4\pi\varepsilon_0}\sum_{\mathbf{n}}\sum_{i=1}^{N}\sum_{j>i}\frac{q_i q_j}{|\mathbf{r}-\mathbf{r}_i+\mathbf{n}L|}\mathrm{erfc}(\frac{|\mathbf{r}-\mathbf{r}_i+\mathbf{n}L|}{\sqrt{2}\sigma}) \tag{3.40}$$

Next, how to derive the long range potential in reciprocal space.The long range force cannot be directly computed in by summation in real space. The basic idea of the Ewald summation is to transform it into a sum in the reciprocal space. For nucleus sitting at certain position, the total charge density field is given by:

$$n^L(\mathbf{r}) = \sum_{n}\sum_{i=1}^{N} n^L(\mathbf{r}+n\mathbf{L}) \tag{3.41}$$

Because the charge density is a periodic function, we can do the Fourier transform of the density and long range potential like what we do in calculating the electronic potential in the above sections. The definition of the Fourier transform we use in this section is shown as following.

$$\begin{aligned} V(\mathbf{r}) &= \sum_{G} V(\mathbf{G})e^{-i\mathbf{G}\cdot\mathbf{r}} \\ V(\mathbf{G}) &= \frac{1}{\Omega}\int V(\mathbf{r}))e^{i\mathbf{G}\cdot\mathbf{r}}d\mathbf{r} \end{aligned} \tag{3.42}$$

The potential field and the charge distribution is related by the Poisson's equation

$$\nabla^2 V^L(\mathbf{r}) = -\frac{n(\mathbf{r})}{\varepsilon_0} \tag{3.43}$$

which can be transformed into reciprocal space (In SI unit)

$$V^L(\mathbf{G}) = \frac{n(\mathbf{G})}{\varepsilon_0 \mathbf{G}^2} \tag{3.44}$$

We use this method to treat the long range potential induced by the Gaussian distribution.

$$n^L(\mathbf{r}) = \sum_n \sum_{j=1}^{N} q_j G(\mathbf{r} - \mathbf{r}_j + n\mathbf{L}) \tag{3.45}$$

$$\begin{aligned}
n^L(\mathbf{G}) =& \frac{1}{\Omega} \int_\Omega \sum_n \sum_{j=1}^{N} q_j G(\mathbf{r} - \mathbf{r}_j + n\mathbf{L}) e^{i\mathbf{G}\mathbf{r}} d\mathbf{r} \\
=& \frac{1}{\Omega} \sum_{j=1}^{N} q_j \int_{R^3} G(\mathbf{r} - \mathbf{r}_j) e^{i\mathbf{G}\mathbf{r}} d\mathbf{r} \\
=& \frac{1}{\Omega} \sum_{j=1}^{N} q_j \int_{R^3} \frac{1}{(2\pi\sigma^2)^{3/2}} \exp[-\frac{(\mathbf{r} - \mathbf{r}_i)^2}{2\sigma^2}] e^{i\mathbf{G}\mathbf{r}} d\mathbf{r} \\
=& \frac{1}{\Omega} \frac{1}{(2\pi\sigma^2)^{3/2}} \sum_{j=1}^{N} q_j \int_{R^3} \exp[-\frac{\mathbf{r}^2}{2\sigma^2}] e^{i\mathbf{G}(\mathbf{r}+\mathbf{r}_j)} d\mathbf{r} \\
=& \frac{1}{\Omega} \sum_{j=1}^{N} q_j e^{i\mathbf{G}\mathbf{r}_j} e^{-\mathbf{G}^2\sigma^2/2}
\end{aligned} \tag{3.46}$$

we get the long range density in Fourier space. Then according to poisson's equation, we can calculate the potential in Fourier space:

$$V^L(\mathbf{G}) = \frac{1}{\varepsilon_0}\frac{1}{\Omega}\sum_{j=1}^{N} q_i e^{i\mathbf{G}\mathbf{r}_j}\frac{e^{-\mathbf{G}^2\sigma^2/2}}{G^2} \tag{3.47}$$

Now applying the inverse Fourier transform to get the potential in real space:

$$V^L(\mathbf{r}) = \frac{1}{\varepsilon_0}\frac{1}{\Omega}\sum_{\mathbf{G}}\sum_{j=1}^{N} q_j e^{i\mathbf{G}(\mathbf{r}_j-\mathbf{r})}\frac{e^{-\mathbf{G}^2\sigma^2/2}}{G^2} \tag{3.48}$$

we can see that the potential decay with the increase of reciprocal vector G, we can ignore the large G term and summation over only small G term. The long-range potential energy is written as:

$$\begin{aligned} E^L &= \frac{1}{2}\sum_{i=1}^{N} q_i V^L(\mathbf{r}_i) \\ &= \frac{1}{2}\frac{1}{\varepsilon_0}\frac{1}{\Omega}\sum_{\mathbf{G}}\sum_{i=1}^{N}\sum_{j=1}^{N} q_i q_j e^{i\mathbf{G}(\mathbf{r}_j-\mathbf{r}_i)}\frac{e^{-\mathbf{G}^2\sigma^2/2}}{G^2} \\ &= \frac{1}{\varepsilon_0}\frac{1}{\Omega}\sum_{\mathbf{G}}\sum_{i=1}^{N}\sum_{j>i} q_i q_j e^{i\mathbf{G}(\mathbf{r}_j-\mathbf{r}_i)}\frac{e^{-\mathbf{G}^2\sigma^2/2}}{G^2} \end{aligned} \tag{3.49}$$

In the last step of derivation, the summation over j have already have no repeat, so we get rid of $1/2$. Defining the structure factor

$$S(\mathbf{G}) = \sum_{i=1}^{N} q_i e^{i\mathbf{G}\mathbf{r}_i} \tag{3.50}$$

$$E^L = \frac{1}{2}\frac{1}{\varepsilon_0}\frac{1}{\Omega}\sum_{\mathbf{G}}\frac{e^{-\mathbf{G}^2\sigma^2/2}}{G^2}|S(\mathbf{G})|^2 \tag{3.51}$$

3.1.6 Short range potential sum in real space

The original form of short range potential can be written as following:

$$V(\mathbf{r}_i - \mathbf{r}_j) = \sum_n \sum_i \sum_{j>i} \frac{Zerfc(\alpha \mathbf{r})}{|\mathbf{r}_i - \mathbf{r}_j + n\mathbf{L}|} \tag{3.52}$$

The cut-off radius for short range potential is $L/2$. At a point r_j, we only consider the particles within the range of $L/2$. The above expression can be simplified, we only consider 1D case. In the code, separate 3D into 3 1D case just like here:

$$V(r) = \sum_i \sum_{j>i} \frac{Zerfc(\alpha r)}{r} \tag{3.53}$$

We can take the derivative with $\mathbf{r}$ to calculate the electric field: in the code there is $1/r$inside the $urtab$, so in the following calculating E field section, we should remember multiply by r

$$E(r) = \sum_i \sum_{j>i} -\frac{Zerfc(\alpha r)}{r^2} + \frac{1}{r}\frac{2}{\sqrt{\pi}}e^{-r^2} \tag{3.54}$$

In this part of implementation, we do not calculating the error function in every loop. Actually, the error function table was initially calculated as a table of 5000. Later on, we choose from the table according to the position differences of two ions. The algorithm (two lines EwaldSumms line 450 451, in this part, many calculations are in this form) for summation of $\sum_i \sum_{j>i}$ is very good.

3.1.7 self energy term and a correction constant

The self potential term is as following, first term is self potential and second is the energy correction which depend on the dipole momentum. If calculate the energy, need to consider $\frac{1}{2}$.

$$V_{self} = \frac{2\alpha Z_i}{\sqrt{\pi}} + \sum_i \frac{\pi Z_i}{\alpha^2 L^3} \tag{3.55}$$

3.1.8 long range potential sum in fourier space

The original long range potential term

$$V_{longrange}(\mathbf{r}) = \frac{4\pi}{L^3} \sum_k \frac{exp(-k^2/4\alpha^2)}{k^2} \sum_j^N q_j e^{i\mathbf{k}\cdot(\mathbf{r}-\mathbf{r}_j)} \tag{3.56}$$

The coefficient should be 4π or 8π depending whether we take spin into account;

$$\begin{aligned} V(\mathbf{r}) &= \frac{4\pi}{L^3} \sum_k \frac{exp(-k^2/4\alpha^2)}{k^2} \sum_{j=1}^N q_j e^{i\mathbf{k}\cdot(\mathbf{r}-\mathbf{r}_j)} \\ &= \frac{4\pi}{L^3} \sum_k \frac{exp(-k^2/4\alpha^2)}{k^2} \sum_{j=1}^N q_j cos(\mathbf{k}\cdot\mathbf{r} - \mathbf{k}\cdot\mathbf{r}_j) \\ &= \frac{4\pi}{L^3} \sum_k \frac{exp(-k^2/4\alpha^2)}{k^2} [cos(\mathbf{k}\cdot\mathbf{r}) \sum_{j=1}^N q_j cos(\mathbf{k}\cdot\mathbf{r}_j) + sin(\mathbf{k}\cdot\mathbf{r}) \sum_{j=1}^N q_j sin(\mathbf{k}\cdot\mathbf{r}_j)] \end{aligned} \tag{3.57}$$

Next, we separate the case of $\mathbf{k}$ into $(k,0,0),(k,l,0),(k,l,m)$. For the first situation $(k,0,0)$. In the $\cos(\mathbf{k}\cdot\mathbf{r})$, we only have one term. The quantity in the code the first dimension represent $k=1$ to $kmax$, second dimension represent X,Y,Z three directions, third dimension represent number of particles. In the $(k,0,0)$ case, we need $(0,l,0)$ $(0,0,m)$, so there is loop of $ic=1$ to 3. For $k=1$ case, we write it $cos(kr)$ explicitly. For other k, we use $sin(kr)$ and $cos(kr)$ to construct the $cos(nkr)$ and $sin(nkr)$. The middle case for example:

$$\begin{aligned} &cos[(k_x,k_y,0)\cdot(r_x,r_y,0)]\sum_{j=1}^{N}q_j cos(\mathbf{k}\cdot\mathbf{r}_j)+sin(\mathbf{k}\cdot\mathbf{r})\sum_{j=1}^{N}q_j sin(\mathbf{k}\cdot\mathbf{r}_j)] \\ =&cos(k_x r_x+k_y r_y)\sum_{j=1}^{N}q_j cos(k_x r_{xj}+k_y r_{yj})+..... \end{aligned} \tag{3.58}$$

since $cos(x+y)$ and $cos(x-y)$ use different rules, we should treat them differently as in the code do. First we calculate the $cos(x+y)$ term, and then we do the summation $\sum_{j=1}^{N}$, then multiply them together and take in to account the difference between $cos(x+y)cos(x-y)$ add them separately. Taking into account all the cases of $(k,0,0),(k,l,0),(k,l,m)$, we can finish the summation. In this way, we avoid double summation. For the summation of k, we choose a maximum $kmax$ value as the cut off.

In the code, we actually calculate the $V(\mathbf{r}_j)$, because we need the $E(\mathbf{r}_j)$ to calculate the force acting on each nucleus. We do not need the potential at each grid.

And in the separate of $\mathbf{k}$, we do not consider $+k$ and $-k$, we only use $+k$, which we should multiply the results by 2.

3.2 Molecular Dynamics

3.2.1 Gaussian isokinetic equation of motion

First, specifying the meaning of two terms:Holonomic and nonholonomic. Holonomic constrains are used to restrict coordinates only do not involve with velocity but nonholonomic is velocity-dependent.

Our definition of temperature is based on the ideal-gas thermometer. Temperature is proportional to the kinetic energy. In non-equilibrium steady state problem, it is convenient to specify the isothermal condition to extract irreversibly generated heat. The multiplier we introduce in the equation of motion plays the role of a friction coefficient, but it takes on both positive and negative value to keep temperature constant.

The Liouville equation describes the evolution of phase space distribution function for the conservative Hamiltonian system. It is the continuity equation for in $6N$ phase space. Let $\rho(q^i, p^i, t)$ denotes the density in phase space. The infinitesimal volume element is $dw = d^{3N}qd^{3N}p$. The surface elements are denote by σ. According to the conservation of mass:

$$\frac{\partial}{\partial t}\int_w \rho dw + \int_\sigma \rho \mathbf{v}\cdot\mathbf{n} d\sigma = 0 \tag{3.59}$$

Using the divergence theory:

$$\frac{\partial}{\partial t}\rho + \nabla\cdot(\rho\mathbf{v}) = 0 \tag{3.60}$$

In $6N$ dimension phase space, the divergence is written as:

$$\frac{\partial \rho}{\partial t} + \sum_{i=1}^{3N}(\frac{\partial \rho}{\partial q_i}\dot{q}_i + \frac{\partial \rho}{\partial p_i}\dot{p}_i) + \sum_{i=1}^{3N}\rho(\frac{\partial \dot{q}_i}{\partial q_i} + \frac{\partial \dot{p}_i}{\partial p_i}) = 0 \tag{3.61}$$

$$\frac{\partial \dot{q}_i}{\partial q_i} = \frac{\partial^2 H(q_i, p_i)}{\partial q \partial p} = -\frac{\partial \dot{p}_i}{\partial p_i} \tag{3.62}$$

In the Hamiltonian system, the last term (compressibility) will vanish, the first two terms will combined into the total derivative. The second term is the Poisson's bracket.

$$\begin{aligned} \frac{d\rho}{dt} &= \frac{\partial \rho}{\partial t} + \sum_{i=1}^{3N} (\frac{\partial \rho}{\partial q_i}\dot{q}_i + \frac{\partial \rho}{\partial p_i}\dot{p}_i) \\ \frac{d\rho}{dt} &= \frac{\partial \rho}{\partial t} + [\rho, H] = 0 \end{aligned} \tag{3.63}$$

Define the operator $L = i[H]$,

$$\begin{aligned} \frac{\partial \rho}{\partial t} + iL\rho = 0 \\ \rho(q,p,t) = &\exp[-iLt]\rho(q,p,0) \end{aligned} \tag{3.64}$$

For the non-Hamiltonian system, the last term (phase space is compressible) will not vanish. We will use the following expression in Isokinetic ensemble.

$$\frac{d\rho}{dt} + \sum_{i=1}^{3N} \rho(\frac{\partial \dot{q}_i}{\partial q_i} + \frac{\partial \dot{p}_i}{\partial p_i}) = 0 \tag{3.65}$$

3.2.2 Gauss's Principle of Least Constraint

According to Gauss's Principle of least constrain, we should first write the constrains function as:

$$g(\mathbf{r}, \dot{\mathbf{r}}, t) = \sum_{i=1}^{N} m_i \dot{\mathbf{r}}_i^2/2 - (3N-1)kT/2 \tag{3.66}$$

Differentiating once with respect to time gives the equation of constraint plane:

$$\sum_{i=1}^{N} m_i \dot{\mathbf{r}}_i \ddot{\mathbf{r}}_i \tag{3.67}$$

Substitute into the Gauss's Principle:

$$\frac{\partial}{\partial \ddot{\mathbf{r}}_i}\Big(\frac{1}{2}\sum_{j=1}^{N} m_j(\ddot{\mathbf{r}}_j - \frac{\mathbf{F}_j}{m_j})^2 + \alpha \sum_{j=1}^{N} m_j \dot{\mathbf{r}}_j \ddot{\mathbf{r}}_j\Big) = 0 \tag{3.68}$$

Finally we get:

$$m_i \ddot{\mathbf{r}}_i = \mathbf{F}_i - \alpha m_i \dot{\mathbf{r}}_i \tag{3.69}$$

Using Hamiltonian we will get the same results:

$$\sum_{i=1}^{N} \mathbf{p}_i^2/2m_i - (3N-1)kT/2 = 0 \tag{3.70}$$

$$g = \sum_{i=1}^{N} \mathbf{p}_i \dot{\mathbf{p}}_i / m_i \tag{3.71}$$

$$\frac{\partial}{\partial \dot{\mathbf{p}}_i} \Big(\frac{1}{2} \sum_{j=1}^{N} m_j (\dot{\mathbf{p}}_j / m_j - \frac{\mathbf{F}_j}{m_j})^2 + \alpha \sum_{i=1}^{N} \mathbf{p}_j \dot{\mathbf{p}}_j / m_j \Big) = 0 \tag{3.72}$$

$$\dot{\mathbf{p}}_i = \mathbf{F}_i - \alpha \mathbf{p}_i \tag{3.73}$$

$$\sum_{i=1}^{N} \mathbf{p}_i \cdot (\mathbf{F}_i - \alpha \mathbf{p}_i) / m_i = 0 \tag{3.74}$$

$$\alpha(\mathbf{q}, \mathbf{p}) = \frac{\sum_{i=1}^{N} \mathbf{F}_i \cdot \mathbf{p}_i / m_i}{\sum_{i=1}^{N} \mathbf{p}_i^2 / m_i} \tag{3.75}$$

3.2.3 Isokinetic ensemble

At equilibrium the Gaussian isokinetic equations become:

$$\begin{aligned} \dot{\mathbf{q}}_i &= \mathbf{p}_i/m = \frac{\partial H}{\partial \mathbf{q}_i} \\ \dot{\mathbf{p}}_i &= \mathbf{F}_i - \alpha \mathbf{p}_i = -\frac{\partial H}{\partial \mathbf{p}_i} - \alpha \mathbf{p}_i \end{aligned} \tag{3.76}$$

From the Liouville's equation, the distribution function can be written as following, and using above expression. In the **fifth** step of derivation, the $\mathbf{p}_i^2/m_i$ is a constant, kinetic energy. In the **seven** step of derivation, $K = 1/2mv^2 = 3/2k_BT$.

$$
\begin{aligned}
\frac{df}{dt} =& -f\frac{\partial}{\partial\Gamma}\cdot\Gamma = -f\sum_{i=1}^{N}(\frac{\partial}{\partial\mathbf{q}_i}\cdot\dot{\mathbf{q}}_i + \frac{\partial}{\partial\mathbf{p}_i}\cdot\dot{\mathbf{p}}_i) \\
=& -f\sum_{i=1}^{N}(\frac{\partial}{\partial\mathbf{q}_i}\cdot\frac{\partial H}{\partial\mathbf{p}_i} + \frac{\partial}{\partial\mathbf{q}_i}\cdot(-\frac{\partial H}{\partial\mathbf{p}_i} - \alpha\mathbf{p}_i)) \\
=& f\sum_{i=1}^{N}\frac{\partial}{\partial\mathbf{p}_i}\cdot(\alpha\mathbf{p}_i) \\
=& f\sum_{i=1}^{N}\frac{\partial}{\partial\mathbf{p}_i}\cdot(\frac{\sum_{i=1}^{N}\mathbf{F}_i\cdot\mathbf{p}_i/m_i}{\sum_{i=1}^{N}\mathbf{p}_i^2/m_i}\mathbf{p}_i) \\
=& 3N\alpha f + (-\alpha) = (3N-1)\alpha f \\
=& (3N-1)(\frac{\sum_{i=1}^{N}\mathbf{F}_i\cdot\mathbf{p}_i/m_i}{\sum_{i=1}^{N}\mathbf{p}_i^2/m_i}\mathbf{p}_i)f \\
=& (3N-1)(\frac{\sum_{i=1}^{N}\mathbf{F}_i\cdot\mathbf{p}_i/m_i}{3NkT}\mathbf{p}_i)f \\
=& (3N-1)(\frac{\sum_{i=1}^{N}-(\partial\phi/\partial t)(\partial t/\partial\mathbf{q})\cdot\mathbf{p}_i/m_i}{3NkT}\mathbf{p}_i)f \\
=& -\frac{(3N-1)}{3NkT}\frac{d\phi}{dt}f
\end{aligned}
\tag{3.77}
$$

In the seven step, if we choose $\sum_{i=1}^{N}\mathbf{p}_i^2/m_i = (3N-1)kT$, we will have simpler expressions:

$$
\begin{aligned}
\frac{d\ \ln f}{dt} =& -\frac{d\phi}{dt} \\
\ln f =& -\frac{\phi}{kT} \\
f(\mathbf{q},\mathbf{p}) =& \exp(\phi/kT)\delta\Big(\sum_{i=1}^{N}\mathbf{p}_i^2/m_i - (3N-1)kT\Big)
\end{aligned}
\tag{3.78}
$$

3.3 Time-Dependent Orbital-Free DFT formalism

3.3.1 Functional derivative

For functions of multiple argument $F[y_0, y_1, y_2.....]$, we can write $dF = \sum_i \frac{\partial F}{\partial y_i} dy_i$. Similarly for functional derivative $F[y(x)]$,

$$\delta F = F[y + \delta y] - F[y] = \int dx \frac{\partial F}{\partial y_i} \delta y_i \tag{3.79}$$

The functional derivative is defined by :

$$F[f(x) + \delta f(x)] - F[f(x)] = \int dx \frac{\delta F[f(x)]}{\delta f(x)} \delta f(x) \tag{3.80}$$

For example, we can do the functional derivative of External potential energy with respect to density:

$$E_{ext}[n(\mathbf{r})] = \int V_{ext}(\mathbf{r}) n(\mathbf{r}) d\mathbf{r} \tag{3.81}$$

$$\begin{aligned} & E_{ext}[n(\mathbf{r}) + \delta n(\mathbf{r})] - E_{ext}[n(\mathbf{r})] \\ = & \int V_{ext}(\mathbf{r})(n(\mathbf{r}) + \delta n(\mathbf{r})) d\mathbf{r} - \int V_{ext}(\mathbf{r}) n(\mathbf{r}) d\mathbf{r} \\ = & \int V_{ext}(\mathbf{r}) \delta n(\mathbf{r}) d\mathbf{r} \end{aligned} \tag{3.82}$$

Compared this expression with the definition, we can see that

$$\frac{\delta F[f(x)]}{\delta f(x)} = V_{ext} \tag{3.83}$$

We lean from this example that if you have a local functional $F[f(x)]$ in the form of a definite integral, we can simply take the derivative of the integrand (a function that is to be integrated) with respect to the function f and get rid of the integral sign.

In the application of potential energy between electrons and ions, it is similar as external potential. We can take derivative of

$$V_{ext}(\mathbf{r})n(\mathbf{r}) \tag{3.84}$$

with respect to $n(\mathbf{r})$, we just get V_{ext}.

In the application of potential energy between electrons and electrons (Hartree Potential energy)

$$E_{Hartree} = \frac{1}{2}\int\int d\mathbf{r}d\mathbf{r}'\frac{n(\mathbf{r})n(\mathbf{r}')}{|\mathbf{r}-\mathbf{r}'|} \tag{3.85}$$

$$
\begin{aligned}
&E_{Hartree}[n(\mathbf{r})+\delta n(\mathbf{r})]-E_{Hartree}[n(\mathbf{r})] \\
=&\frac{1}{2}\int\int d\mathbf{r}d\mathbf{r}'\frac{(n(\mathbf{r})+\delta n(\mathbf{r}))(n(\mathbf{r}')+\delta n(\mathbf{r}'))}{|\mathbf{r}-\mathbf{r}'|}-\frac{1}{2}\int\int d\mathbf{r}d\mathbf{r}'\frac{n(\mathbf{r})n(\mathbf{r}')}{|\mathbf{r}-\mathbf{r}'|} \\
=&\frac{1}{2}\int\int d\mathbf{r}d\mathbf{r}'\frac{\delta n(\mathbf{r})n(\mathbf{r}')+\delta n(\mathbf{r}')n(\mathbf{r})}{|\mathbf{r}-\mathbf{r}'|} \\
=&\int\int d\mathbf{r}d\mathbf{r}'\frac{\delta n(\mathbf{r})n(\mathbf{r}')}{|\mathbf{r}-\mathbf{r}'|}
\end{aligned}
\tag{3.86}
$$

Consider the symmetry of $n(\mathbf{r})$ and $n(\mathbf{r}')$, we can conduct the last step of above derivation. Comparing with the definition of functional derivative, we can get the result:

$$
\int d\mathbf{r}'\frac{n(\mathbf{r}')}{|\mathbf{r}-\mathbf{r}'|}=V_{Hartree} \tag{3.87}
$$

3.3.2 Thomas-Fermi kinetic energy functional

In this section, we will derive the Thomas-Fermi functional. The number of particles N in the system can be written in this form :

$$
N=\int a(\varepsilon)f(\varepsilon)d\varepsilon \tag{3.88}
$$

where $a(\varepsilon)$ is the density of the states, $f(\varepsilon)$ is the particle distribution. In this case, it is just Fermi-Dirac distribution. The density of states of non-interacting Fermi gas can be written as:

$$\begin{aligned} a(p) &= 2 * \frac{V}{h^3} 4\pi p^2 dp \\ a(\varepsilon) &= 2 * \frac{V}{h^3} 2\pi (2m)^{3/2} \varepsilon^{1/2} d\varepsilon \end{aligned} \tag{3.89}$$

Taking into account of Fermi-Dirac distribution, the number of particles can is :

$$N = \int 2 * \frac{V}{h^3} 2\pi (2m)^{3/2} \varepsilon^{1/2} \frac{1}{exp[(\varepsilon - u)/kT] + 1} d\varepsilon \tag{3.90}$$

After change of variable $x = \varepsilon/kT$ and fugacity $z = exp[u/kT]$, we get

$$\begin{aligned} \frac{N}{V} &= 2 * \frac{2\pi}{h^3} (2mkT)^{3/2} \int \frac{x^{1/2}}{z^{-1}e^x + 1} dx \\ &= \frac{4\pi}{\hbar^3 (2\pi)^3} (2mkT)^{3/2} \int \frac{x^{1/2}}{z^{-1}e^x + 1} dx \\ &= (\frac{m}{\hbar^2})^{3/2} \frac{\sqrt{2}}{\pi^2 \beta^{3/2}} \int \frac{x^{1/2}}{z^{-1}e^x + 1} dx \end{aligned} \tag{3.91}$$

Using the relation

$$\begin{aligned} \frac{PV}{kT} = ln\Xi &= \int a(\varepsilon) ln(1 + ze^{\beta\varepsilon}) d\varepsilon \\ &= \frac{2}{3} V (\frac{m}{\hbar^2})^{3/2} \frac{\sqrt{2}}{\pi^2 \beta^{3/2}} \int \frac{x^{3/2}}{z^{-1}e^x + 1} dx \end{aligned} \tag{3.92}$$

And use the relation of thermal dynamics:

$$\begin{aligned} U = -\frac{\partial}{\partial\beta} ln\Xi =& kT^2[\frac{\partial}{\partial T}(\frac{PV}{kT})] \\ =& \frac{3}{2}kT\frac{2}{3}V(\frac{m}{\hbar^2})^{3/2}\frac{\sqrt{2}}{\pi^2\beta^{3/2}}\int\frac{x^{3/2}}{z^{-1}e^x+1}dx \\ =& V(\frac{m}{\hbar^2})^{3/2}\frac{\sqrt{2}}{\pi^2\beta^{5/2}}\int\frac{x^{3/2}}{z^{-1}e^x+1}dx \\ =& \frac{3}{2}PV \end{aligned} \tag{3.93}$$

According to Euler's equation:

$$U = TS - PV + \mu N \tag{3.94}$$

and the definition of Helmholtz Free energy;

$$\begin{aligned} A =& U - TS \\ =& -PV + \mu N \\ =& -\frac{2}{3}U + \mu N \end{aligned} \tag{3.95}$$

Finally we get the density of free energy:

$$
\begin{aligned}
\frac{A}{V} &= -\frac{2}{3}(\frac{m}{\hbar^2})^{3/2}\frac{\sqrt{2}}{\pi^2\beta^{5/2}}\int\frac{x^{3/2}}{z^{-1}e^x+1}dx+\mu\frac{N}{V} \\
&= -\frac{2}{3}(\frac{m}{\hbar^2})^{3/2}\frac{\sqrt{2}}{\pi^2\beta^{5/2}}\int\frac{x^{3/2}}{z^{-1}e^x+1}dx+\mu*(\frac{m}{\hbar^2})^{3/2}\frac{\sqrt{2}}{\pi^2\beta^{3/2}}\int\frac{x^{1/2}}{z^{-1}e^x+1}dx \\
&= -\frac{2}{3}(\frac{m}{\hbar^2})^{3/2}\frac{\sqrt{2}}{\pi^2\beta^{5/2}}I_{3/2}+\mu*(\frac{m}{\hbar^2})^{3/2}\frac{\sqrt{2}}{\pi^2\beta^{3/2}}I_{1/2} \\
&= -\frac{2}{3}(\frac{m}{\hbar^2})^{3/2}\frac{\sqrt{2}}{\pi^2\beta^{5/2}}I_{3/2}+\beta\mu*(\frac{m}{\hbar^2})^{3/2}\frac{\sqrt{2}}{\pi^2\beta^{5/2}}I_{1/2} \\
&= (\frac{m}{\hbar^2})^{3/2}\frac{\sqrt{2}}{\pi^2\beta^{5/2}}(-\frac{2}{3}I_{3/2}+\beta\mu I_{1/2})
\end{aligned}
\tag{3.96}
$$

Where we defined

$$
\begin{aligned}
\frac{N}{V} &= (\frac{m}{\hbar^2})^{3/2}\frac{\sqrt{2}}{\pi^2\beta^{3/2}}\int\frac{x^{1/2}}{z^{-1}e^x+1}dx \\
&= (\frac{m}{\hbar^2})^{3/2}\frac{\sqrt{2}}{\pi^2\beta^{3/2}}I_{1/2}
\end{aligned}
\tag{3.97}
$$

Where we defined the Thomas function different from Pathria's book.

$$
I_{1/2} = \int\frac{x^{1/2}}{z^{-1}e^x+1}dx \tag{3.98}
$$

Next we try to find the analytical expression for free energy.

First, Fermi energy in this case can be written as (Pathria (8.1.24)) :

$$\varepsilon_F = (\frac{6\pi^2 n}{2})^{2/3}\frac{\hbar}{2m} \tag{3.99}$$

We can define the reduced temperature:

$$t = \frac{T}{T_f} = \frac{2}{\beta[3\pi^2 n]^{2/3}}\frac{m}{\hbar} \tag{3.100}$$

Then the equation for density can be expressed as

$$y = I_{1/2}(\beta\mu) = (\frac{\hbar^2}{m})^{3/2}\frac{\pi^2}{\sqrt{2}}\beta^{3/2}n = \frac{2}{3t^{3/2}} \tag{3.101}$$

Next define a function $f(\eta)$, where $\eta = \beta\mu$

$$f(\eta) = \frac{\beta A/V}{N/V} = \frac{1}{I_{1/2}(\eta)}[-\frac{2}{3}I_{3/2}(\eta) + \beta\mu I_{1/2}(\eta)] \tag{3.102}$$

Once we know the density, we can calculate the y immediately. And y is related to η by $I_{1/2}$, from which we can get $\eta(y)$.The series expansion for $I_\alpha(\eta)$ can be expressed as:

$$I_\alpha(\eta) = \Gamma(\alpha+1)e^\eta \sum_{k=0}^{\infty}(-1)^k \frac{e^{k\eta}}{(k+1)^{\alpha+1}} \tag{3.103}$$

For example, in the non-degenerate limit (Temperature very high and density very low, $Z << 1$ and chemical potential μ must be negative and magnitude large to make Z approach zero, classical limit).

$$y = I_{1/2}(\eta) \approx= \frac{\sqrt{\pi}}{2} e^\eta (1 - \frac{e^\eta}{2\sqrt{2}}) \tag{3.104}$$

From this equation, we can solve for η in terms of y.

$$\eta(y) = ln(\frac{2}{\sqrt{\pi}}y) + \frac{y}{\sqrt{2\pi}} + O(y^2) \tag{3.105}$$

Substitute the η in to the $f(\eta)$, we can finally get the Free energy A/V of the system. Similarly, we can get the degenerate limit $Z >> 1$ expressions (for bosons, $0 < Z < 1$). The relation between the Energy and the Density should be fitted through polynomials or other analytical functions.

Free energy per unit volume (Free energy density) is written as, is what we see in the code.

$$\frac{A}{V} = \frac{nf(y)}{\beta} \tag{3.106}$$

In the code, we use the integral function to get the total free TF energy.

$$A = \int (\frac{A}{V}) dV = \sum_{N_x, N_y, N_z} \frac{A}{V} \frac{V}{N_x * N_y * N_z} \tag{3.107}$$

We do the integration in real space, it is the standard definition of integration. In the code, there is also function called Fintegral to calculate the integration in Fourier space. We use this to calculate the potential energy in Fourier space.

In the minimization process, we use the free energy of the system to take the functional derivative.

$$\begin{aligned} \frac{\partial A}{\partial n} &= \frac{f(y)}{\beta} + \frac{\partial f(y)}{\partial y} \frac{\partial y}{\partial n} \\ &= \frac{f(y)}{\beta} + \frac{\partial f(y)}{\partial y} (\frac{\hbar^2}{m})^{3/2} \frac{\pi^2}{\sqrt{2}} \beta^{3/2} \\ &= \frac{f(y)}{\beta} + \frac{\partial f(y)}{\partial y} * \text{factor} \end{aligned} \tag{3.108}$$

This is exactly what we see in the code, where the factor is $(\frac{\hbar^2}{m})^{3/2} \frac{\pi^2}{\sqrt{2}} \beta^{3/2}$.

In the code, the kinetic energy is also calculated

$$A = U - TS \tag{3.109}$$

For ideal Fermi system, we do not have potential energy, we only have kinetic energy.

$$A = K - TS \tag{3.110}$$

Since entropy S is independent of temperature we can calculate the kinetic energy in the following way.

$$K = \frac{\partial(\beta A)}{\partial \beta} = \frac{\partial(\beta K - kS)}{\partial \beta} \tag{3.111}$$

Actually, it is just the U we calculated in the above sub-section.

$$\begin{aligned} K = \frac{\partial(\beta A)}{\partial \beta} = \frac{\partial(nf(y))}{\partial \beta} &= n\frac{\partial(f(y))}{\partial y}\frac{\partial(y)}{\partial \beta} \\ &= n\frac{\partial(f(y))}{\partial y} n\frac{\partial factor}{\partial \beta} \end{aligned} \tag{3.112}$$

This expression is just what we see in the code.

3.3.3 Von Weizsäcker kinetic energy functional

This term is exact for any single orbital system, i.e., for up to two singlet-coupled fermions or any number of bosons. The vW functional by it self is a lower bound to the true kinetic energy since it neglects spin and Pauli Exclusion Principle. Imposition of the Pauli Principle for more than two electrons introduces the nodes in the many-body wave function, which increase the kinetic energy. For a one-orbital system,the kinetic energy can be calculated exactly, the first step derivation using integral by part and Gaussian' theory, the surface term vanish:

$$\begin{aligned} F_{vw} &= -\frac{1}{2}\int d\mathbf{r}\varphi(\mathbf{r}^*)\nabla^2\varphi(\mathbf{r}) \\ &= \frac{1}{2}\int d\mathbf{r}|\nabla\varphi(\mathbf{r})|^2 \\ &= \frac{1}{2}\int d\mathbf{r}|\nabla\sqrt{n}||\nabla\sqrt{n}| \\ &= \frac{1}{8}\int d\mathbf{r}\frac{|\nabla\sqrt{n}|^2}{n(r)} \end{aligned} \tag{3.113}$$

Taking into account the first gradient correction lead to the free energy:

$$F_w = \int h(n)\frac{|\nabla n(r)|^2}{n(r)}dr \tag{3.114}$$

The $h(n)$ is given in F. Perrot (PRA 1979) by identifying the polarizability of a system with exact polarizability of the non interacting electron gas at

large wavelength.

$$\frac{|\nabla n(r)|^2}{n(r)} = \frac{|\nabla \psi^2(r)|^2}{\psi^2(r)} = \frac{|2\psi(r)\nabla\psi(r)|^2}{\psi^2(r)} = 4|\nabla\psi(r)|^2 \tag{3.115}$$

In the code, calculating the square of the gradient in Fourier space $(-iG\psi(G))$. The above expression is exact what we use to calculate the free energy in the code. Next, we calculate the functional derivative:

$$\frac{F[f, f']}{\delta f} = \frac{\partial a}{\partial f} - \frac{d}{dx}\frac{\partial a}{\partial f'} \tag{3.116}$$

where a is the kernel of a integral, using this relation, it is simple to get functional derivative of above equation, take h as $1/8$. First term goes to zero because is independent of ψ, the ψ, ψ' is independent of each other.

$$\frac{\partial F_w}{\delta\psi} = \frac{1}{2}\frac{\partial(|\nabla\psi(r)|^2)}{\partial\psi} - \frac{1}{2}\frac{d}{dx}\frac{\partial|\nabla\psi(r)|^2}{\partial\psi'} = -\nabla^2\psi(r) \tag{3.117}$$

$$\begin{aligned}
\frac{\delta F_w}{\delta n} =& \frac{\partial}{\partial n}(h(n)\frac{|\nabla n(r)|^2}{n(r)}) \\
=& |\nabla n(r)|^2\frac{\partial}{\partial n}(\frac{h}{n}) + \frac{h}{n}\frac{\partial}{\partial n}|\nabla n(r)|^2 \\
=& |\nabla n(r)|^2(\frac{(\partial h/\partial n)n - h}{n^2}) + \frac{h}{n}2\frac{\partial n}{\partial r}\frac{\partial^2}{\partial^2 r}\frac{\partial r}{\partial n} \\
=& |\nabla n(r)|^2(\frac{(\partial h/\partial n)n - h}{n^2}) + 2\frac{h}{n}\nabla^2 n
\end{aligned} \tag{3.118}$$

If we take derivative with ψ, we should multiply the above equation by 2ψ.

$$\begin{aligned}
\frac{\delta F_w}{\delta \psi} =& \Big(|\nabla n(r)|^2(\frac{(\partial h/\partial \psi)n/2\psi - h}{n^2}) + 2\frac{h}{n}\nabla^2 n\Big)2\psi \\
=& \Big(4\psi^2|\nabla\psi|^2(\frac{(\partial h/\partial \psi)\psi/2 - h}{\psi^4}) + 2h\frac{2|\nabla\psi|^2 + 2\psi\nabla^2\psi}{\psi^2}\Big)2\psi \\
=& 8\Big(|\nabla\psi|^2\frac{\partial h}{\partial \psi}\psi/2 + h\nabla^2\psi\Big) \\
=& 8\Big(|\nabla\psi|^2\frac{\partial h}{\partial n} + h\nabla^2\psi\Big) \\
=& 8\Big(|\nabla\psi|^2\frac{\partial h}{\partial y} * \text{factor} + h\nabla^2\psi\Big)
\end{aligned} \tag{3.119}$$

Since $y = (\frac{\hbar^2}{m})^{3/2}\frac{\pi^2}{\sqrt{2}}\beta^{3/2}n$, where the factor is $(\frac{\hbar^2}{m})^{3/2}\frac{\pi^2}{\sqrt{2}}\beta^{3/2}$.

For the final calculation, we calculating the kinetic energy of the system in the same way as we use in TF case:

$$\begin{aligned}
K = \frac{\partial(\beta F_w)}{\partial \beta} =& F_w + \beta\frac{\partial\Big(h(n)\frac{|\nabla n(r)|^2}{n(r)}\Big)}{\partial\beta} \\
=& F_w + \beta 4|\nabla\psi(r)|^2\frac{\partial h}{\partial y}\frac{\partial y}{\partial \beta} \\
=& F_w + 4\frac{\partial h}{\partial y}|\nabla\psi(r)|^2\frac{3}{2}
\end{aligned} \tag{3.120}$$

This expression is just what we see in the code.

3.3.4 Free energy minimization and OF equation

The free energy of the system is written as:

$$F[n(\mathbf{r})] = F_{TF..} + \int V_{ext} n(\mathbf{r}) d\mathbf{r} + \frac{1}{2} \int \int d\mathbf{r} d\mathbf{r'} \frac{n(\mathbf{r}) n(\mathbf{r'})}{|\mathbf{r} - \mathbf{r'}|} + F_{xc} \tag{3.121}$$

Introducing another quantities that related to density by : Attention norm square

$$n(\mathbf{r}) = |\psi(\mathbf{r})|^2 \tag{3.122}$$

The equation of free energy is constrained by condition:

$$\int |\psi(\mathbf{r})|^2 d\mathbf{r} = N \tag{3.123}$$

Taking the constrains into account by Lagrange's multiplier, we get :

$$\begin{aligned} W[\psi(\mathbf{r})] = F_{TF..} + \int V_{ext} n(\mathbf{r}) d\mathbf{r} + \frac{1}{2} \int \int d\mathbf{r} d\mathbf{r'} \frac{n(\mathbf{r}) n(\mathbf{r'})}{|\mathbf{r} - \mathbf{r'}|} + F_{xc} \\ - \mu [\int \psi(\mathbf{r})^2 d\mathbf{r} - N] \end{aligned} \tag{3.124}$$

where μ is the chemical potential.

$$\begin{aligned}\frac{\delta W[\psi(\mathbf{r})]}{\delta\psi(\mathbf{r})} =& \frac{\delta F[\psi(\mathbf{r})]}{\delta n(\mathbf{r})}\frac{\delta n(\mathbf{r})}{\delta\psi(\mathbf{r})} - 2\mu\psi(\mathbf{r}) \\ =& 2[\frac{\delta F[\psi(\mathbf{r})]}{\delta n(\mathbf{r})} - \mu]\psi(\mathbf{r}) \\ =& 2[\frac{\delta F_{TF}}{\delta n(\mathbf{r})} + \lambda\frac{\delta F_W}{\delta n(\mathbf{r})} + \frac{\delta F_{xc}}{\delta n(\mathbf{r})} + V_{ext} + \int d\mathbf{r}'\frac{n(\mathbf{r}')}{|\mathbf{r}-\mathbf{r}'|} - \mu]\psi(\mathbf{r})\end{aligned} \tag{3.125}$$

Where λ is introduced to correct the overestimation of the von-Weizsacker term. And in the first step of derivation, we use the definition of functional derivative.

In the code. The first three terms are kinetic terms and exchange correlation terms. The last term is $2\psi(\mathbf{r})V(\mathbf{r})$, which take into account that density is $\psi(\mathbf{r})^2$. In the minimization subroutine, the dFdpsi is called Hamiltonian. Multiply by L^3 is because we calculated the potential per unit volume. For example, the free energy A/V.

$$\frac{\delta W}{\delta\psi(\mathbf{r})} = 2\lambda(H\psi(\mathbf{r}) - \mu\psi(\mathbf{r})) = 0 \tag{3.126}$$

Where H is

$$H(\psi(\mathbf{r}) = -\frac{1}{2}\nabla^2 + \frac{1}{\lambda}[\frac{\delta F_{TF}}{\delta n(\mathbf{r})} + \frac{\delta F_{xc}}{\delta n(\mathbf{r})} + V_{ext} + \int d\mathbf{r}'\frac{n(\mathbf{r}')}{|\mathbf{r}-\mathbf{r}'|}] \tag{3.127}$$

Finally, we get the same form as the KS equations.

$$H\psi(\mathbf{r}) = \mu\psi(\mathbf{r})) \tag{3.128}$$

3.3.5 Conjugate Gradient for Optimization

Take the bra product from left of above equation:

$$\langle\psi|\,\hat{H}\,|\psi\rangle = \langle\psi|\,\mu\,|\psi\rangle = N\mu \tag{3.129}$$

Chemical potential is calculated as:

$$\mu = \frac{\int d\mathbf{r}\psi(\mathbf{r})H\psi(\mathbf{r})}{N} \tag{3.130}$$

The SD (steepest descent) vector is calculated as : just the negative of gradient vector.

$$\zeta = \frac{\delta W}{\delta\psi(\mathbf{r})} = 2\lambda(\mu - H)\psi(\mathbf{r}) \tag{3.131}$$

In the first step, we have to use SD vector as CG vector. We use ϕ denotes the CG vector, ζ as SD vector, φ as wave function, W total energy of the system.

$$|\phi_0\rangle = |\zeta_0\rangle = \frac{\delta W_0}{\delta\,\langle\psi_0(\mathbf{r})|} = \frac{\delta W_0}{\delta n}\frac{\delta n}{\delta\,\langle\psi_0(\mathbf{r})|} = 2\lambda(\mu_0 - H_0)\,|\psi_0(\mathbf{r})\rangle \tag{3.132}$$

Attention here we minimize with respect to $\langle\psi_0(\mathbf{r})|$ in order to get the results

vector in $|ket\rangle$ form. Since

$$n(\mathbf{r}) = |\psi(\mathbf{r})|^2 = \psi^*(\mathbf{r})\psi(\mathbf{r}) \tag{3.133}$$

$$\langle\psi(\mathbf{r})|\psi(\mathbf{r})\rangle = \int \psi^*(\mathbf{r})\psi(\mathbf{r})d\mathbf{r} = N \tag{3.134}$$

The CG vector must be further orthogonalized to wave function ψ_i and normalized to N.

$$\phi_0' = (1 - \frac{|\psi_0\rangle\langle\psi_0|}{N})\,|\phi\rangle \tag{3.135}$$

$$|\phi_0''\rangle = \sqrt{\frac{N}{\langle\phi_0'|\phi_0'\rangle}}\,|\phi_0'\rangle \tag{3.136}$$

After get the normalized CG vector ϕ_0'', we can update the wave function φ through the direction of CG vector.

$$|\psi_1\rangle = |\psi_0\rangle\, cos\theta_0 + |\phi_0''\rangle\, sin\theta_0 \tag{3.137}$$

Where the value of θ is determined by minimizing the total energy as the function of θ. The following two subroutines are the detailed process to calculate the minimum θ.

After know the minimum θ. we can update the wave function, free energy, chemical potential and so on.

$$\mu_1 = \frac{\int d\mathbf{r}\psi_1(\mathbf{r})H\psi_1(\mathbf{r})}{N} \tag{3.138}$$

$$|\zeta_1\rangle = \frac{\delta W_1}{\delta\psi_1(\mathbf{r})} = 2\lambda(\mu_1 - H_1)\,|\psi_1(\mathbf{r})\rangle \tag{3.139}$$

$$|\phi_1\rangle = |\zeta_1\rangle + \frac{\langle\zeta_1|\zeta_1\rangle}{\langle\zeta_0|\zeta_0\rangle}\,|\phi_0\rangle \tag{3.140}$$

After normalization, we can update the wave function again. The we repeat the second step minimization process.

$$|\psi_2\rangle = |\psi_1\rangle\, cos\theta_1 + |\phi_1''\rangle\, sin\theta_1 \tag{3.141}$$

Compared to standard Conjugate Gradient method, we update the CG vector ϕ in the same way. However, we update the wave function ψ in a different way from the CG method. We minimize with respect to θ. But the spirit of the method is the same, so i guess the process will terminate in N steps.

At the end of this section, I want to summarize the rank of CG vector. In 2D case (x_1, x_2) , when we minimize with respect to vector $\mathbf{x} = (x_1, x_2)$, the CG vector is also a 2*2 vector.

$$-f'(x) = [\frac{\partial f(x)}{\partial x_1}, \frac{\partial f(x)}{\partial x_2}] \tag{3.142}$$

In our minimization, we minimize with respect to a matrix, so I wonder how many steps we need to finish the minimization process. The Free Energy of

the whole system (entire box) is only a number, it depends on the summation of density, and density depend on the coordinates x, y, z.

Mnbrak finds 3 points of a function bracketing a minimum, giving two initial points ax bx. It searches in the downward direction until it can find three new values ax bx cx that bracket a minimum. In this subroutine, we use Parabolic Interpolation to find the minimum.

The function $f(x)$ can be approximated by a parabola (quadratic function) in the neighborhood of its minimum (or maximum). Let $a < b < c$ be three points on the x-axis corresponding to function values $f(a) > f(b) < f(c)$. Then a quadratic function can be generated through these points by the Lagrange interpolation:

$$q(x) = f(a)\frac{(x-b)(x-c)}{(a-b)(a-c)} + f(b)\frac{(x-c)(x-a)}{(b-c)(b-a)} + f(c)\frac{(x-a)(x-b)}{(c-a)(c-b)}$$

To find the minimum $q(x)$ at the vertex of this quadratic function, we set its derivative to zero $q'(x) = 0$ and get:

$$q'(x) = f(a)\frac{(x-b)+(x-c)}{(a-b)(a-c)} + f(b)\frac{(x-c)+(x-a)}{(b-c)(b-a)} + f(c)\frac{(x-a)+(x-b)}{(c-a)(c-b)} = 0$$

Multiplying both sides by $(a-b)(b-c)(c-a)$ we get

$$f(a)(c-b)(2x-b-c) + f(b)(a-c)(2x-c-a) + f(c)(b-a)(2x-a-b) = 0$$

i.e.,

$$2x[f(a)(c-b)+f(b)(a-c)+f(c)(b-a)]-[f(a)(c^2-b^2)+f(b)(a^2-c^2)+f(c)(b^2-a^2)]=0$$

Solving for x we get:

$$\begin{aligned}
x_{min} &= \frac{1}{2}\frac{f(a)(c^2-b^2)+f(b)(a^2-c^2)+f(c)(b^2-a^2)}{f(a)(c-b)+f(b)(a-c)+f(c)(b-a)} \\
&= b+\frac{1}{2}\frac{f(a)(c-b)(c+b-2b)+f(b)(a-c)(a+c-2b)+f(c)(b-a)(b+a-2b)}{f(a)(c-b)+f(b)(a-c)+f(c)(b-a)} \\
&= b+\frac{1}{2}\frac{f(a)(c-b)^2+f(b)(a-c)(a+c-2b)-f(c)(b-a)^2}{f(a)(c-b)+f(b)(a-c)+f(c)(b-a)} \\
&= b+\frac{1}{2}\frac{[f(a)-f(b)](c-b)^2-[f(c)-f(b)](b-a)^2}{[f(a)-f(b)](c-b)+[f(c)-f(b)](b-a)}
\end{aligned}$$

It is the u we see in the code. When the $f(a) > f(b) < f(c)$, we bracket the minimum and finish this subroutine.

Since we already have $f(a) > f(b) < f(c)$, we can use parabolic to fit the function and find the minimum value of θ. we can substitute the three numbers into the parabolic equations and solve the determinant of the matrix to get the parameter of parabolic functions.

3.3.6 Time evolution of collective orbital

We use splitting techniques to do the time propagator. The split-operator(SO) techniques takes advantage of the fact that the Hamiltonian is composed of two terms, one diagonal in Fourier space(kinetic term) and potential term

diagonal in real space.The time dependent Schrodinger equation in atomic unit in 1D:

$$-\frac{1}{2}\nabla^2\psi(x,t) + V(x)\psi(x,t) = i\frac{\partial\psi(x,t)}{\partial t} \tag{3.143}$$

which have a solution

$$\psi(x,t) = \exp\Big(-i(-\frac{1}{2}\nabla^2 + V(x))\Delta t)\Big)\psi(x,0) \tag{3.144}$$

Splitting the Laplacian operator into two parts:

$$\psi(x,t) = \exp[i(\frac{1}{4}\nabla^2\Delta t)]\exp[-iV(x)\Delta t)]\exp[i(\frac{1}{4}\nabla^2\Delta t)]\psi(x,0) \tag{3.145}$$

This decomposition neglects the commutator term of x and p, and accuracy of this method is $(\Delta t)^2$. In Fourier space, the Laplacian operator acts as $(iG)^2$ where G is the reciprocal vector. So in the codes, I do the loop as following :

1. First Fourier transform $\psi(x,0)$ into $F\psi(G,0)$ in fourier space
2. Propagate $F\psi(G,0)$ in half step:

$$F\psi(x,\Delta t/2) = \exp[-\frac{i}{4}G^2\Delta t]F\psi(x,0) \tag{3.146}$$

3. transform back to real space $\psi(x,\Delta t/2)$
4. Propagate $\psi(G,\Delta t/2)$ in full one step in real space:

$$\psi(x, \Delta t/2) = \exp[-iV(x)\Delta t]\psi(x, \Delta t/2) \tag{3.147}$$

5. Fourier transform $\psi(x, \Delta t/2)$ again into $F\psi(G, \Delta t/2)$ in fourier space
6. Propagate $F\psi(G, \Delta t/2)$ in half step:

$$F\psi(x, \Delta t) = \exp[-\frac{i}{4}G^2\Delta t]F\psi(x, \Delta t/2) \tag{3.148}$$

7. Transform back to real space we get the $\psi(x, \Delta t)$

During this process, the value of G is range from 0 128 -127 -1, this is typical $fftw$ use to do fft. However, if you use python scipy.fftpack, the G vector is 0 127 -128 -1. Python numpy is also different from these two. When use the fft to solve Possion's equation, the $G = 0$ is set to zero to avoid division by zero. In the time propagator part, I rewrite a subroutine TD_Reciprocal_vector in which the G is normal, do not set zero.

Next, the Kohn Sham Hamiltonian (actually chemical potential according to scaling) we use now to do the propagator. This Hamiltonian is derived as:

$$H(\psi(\mathbf{r})) = -\frac{1}{2}\nabla^2 + [\frac{\delta F_{TF}}{\delta n(\mathbf{r})} + \frac{\delta F_{xc}}{\delta n(\mathbf{r})} + V_{ext} + \int d\mathbf{r}'\frac{n(\mathbf{r}')}{|\mathbf{r} - \mathbf{r}'|}] \tag{3.149}$$

In the propagator, the first term work as kinetic operator, the following four term work together as the potential term.

The derivation of the first term is as following: This term is exact for

any single orbital system, i.e., for up to two singlet-coupled fermions or any number of bosons. The vW functional by it self is a lower bound to the true kinetic energy since it neglects spin and Pauli Exclusion Principle. Imposition of the Pauli Principle for more than two electrons introduces the nodes in the many-body wave function, which increase the kinetic energy. For a one-orbital system,the kinetic energy can be calculated exactly, the first step derivation using integral by part and Gaussian' theory, the surface term vanish:

$$\begin{aligned} F_{vw} &= -\frac{1}{2}\int d\mathbf{r}\varphi(\mathbf{r}^*)\nabla^2\varphi(\mathbf{r}) \\ &= \frac{1}{2}\int d\mathbf{r}|\nabla\varphi(\mathbf{r})|^2 \\ &= \frac{1}{2}\int d\mathbf{r}|\nabla\sqrt{n}||\nabla\sqrt{n}| \\ &= \frac{1}{8}\int d\mathbf{r}\frac{|\nabla\sqrt{n}|^2}{n(r)} \end{aligned} \tag{3.150}$$

Taking into account the first gradient correction lead to the free energy:

$$F_w = \int h(n)\frac{|\nabla n(r)|^2}{n(r)}dr \tag{3.151}$$

The $h(n)$ is calcuated by identifying the polarizability of a system with exact polarizability of the non interacting electron gas at large wavelength.

$$\frac{|\nabla n(r)|^2}{n(r)} = \frac{|\nabla \psi^2(r)|^2}{\psi^2(r)} = \frac{|2\psi(r)\nabla\psi(r)|^2}{\psi^2(r)} = 4|\nabla\psi(r)|^2 \tag{3.152}$$

In the code, calculating the square of the gradient in Fourier space $(-iG\psi(G))$. The above expression is exact what we use to calculate the free energy in the code. Next, we calculate the functional derivative:

$$\frac{F[f, f']}{\delta f} = \frac{\partial a}{\partial f} - \frac{d}{dx}\frac{\partial a}{\partial f'} \tag{3.153}$$

where a is the kernel of a integral, using this relation, it is simple to get functional derivative of above equation, take h as $1/8$. First term goes to zero because is independent of ψ, the ψ, ψ' is independent of each other.

$$\frac{\partial F_w}{\delta\psi} = \frac{1}{2}\frac{\partial(|\nabla\psi(r)|^2)}{\partial\psi} - \frac{1}{2}\frac{d}{dx}\frac{\partial|\nabla\psi(r)|^2}{\partial\psi'} = -\nabla^2\psi(r) \tag{3.154}$$

pay attention to multiply by 2 $/psi$ or not in the code.

3.4 Current dependent kinetic energy functional

3.4.1 Linear response theory and Lindhard function

In terms of Linear Response (LR) theory, a small change in the potential causes a first order change in density:

$$\partial\rho(\mathbf{r},t) = \int d\mathbf{r}' \int dt' \chi(\mathbf{r},\mathbf{r}',t,t')\partial V(\mathbf{r}',t') \tag{3.155}$$

$$\chi(\mathbf{r},\mathbf{r}',t,t')^{-1} = -\frac{\partial V(\mathbf{r}',t')}{\partial\rho(\mathbf{r},t)} = -\frac{\partial^2 E(\rho)}{\partial\rho(\mathbf{r},t)\partial\rho(\mathbf{r}',t')} \tag{3.156}$$

In Fourier Space :

$$\tilde{\chi}(\mathbf{r},\mathbf{q},t,\omega)^{-1} = -\mathcal{F}[\frac{\partial^2 E(\rho)}{\partial\rho(\mathbf{r},t)\partial\rho(\mathbf{r}',t')}] \tag{3.157}$$

Lindhard static response function $\omega = 0$

Start from the simple static case in free electron gas limit, the density ρ is uniform, orbitals $\phi_{\mathbf{k}}(\mathbf{r})$ are plane waves :

$$\phi_{\mathbf{k}}(\mathbf{r}) = (\frac{1}{2\pi})^{-3/2} e^{i\mathbf{k}\cdot\mathbf{r}} \tag{3.158}$$

Introduce a weak perturbation potential $V(\mathbf{r})$ into this system, first order the orbitals can be written accurately as :

$$\phi_{\mathbf{k}}^{(1)}(\mathbf{r}) = \phi_{\mathbf{k}}(\mathbf{r}) + \sum_{k \neq k} \frac{V_c}{\epsilon_k - \epsilon_{k'}} \phi_{\mathbf{k}'}(\mathbf{r}) \tag{3.159}$$

where V_c is the coupling element give by :

$$V_c = (2\pi)^{-3} \tilde{V}(\mathbf{k} - \mathbf{k}') \tag{3.160}$$

Introducing a new variable $\mathbf{q} = \mathbf{k} - \mathbf{k}'$ and replace the summation with integration :

$$\phi_{\mathbf{k}}^{(1)}(\mathbf{r}) = \phi_{\mathbf{k}}(\mathbf{r}) + \frac{2}{2\pi^3} \int_{q \neq 0} \frac{\tilde{V}(\mathbf{q}) \phi_{k-q}(\mathbf{r})}{\mathbf{k}^2 - (\mathbf{k} - \mathbf{q})^2} d\mathbf{q} \tag{3.161}$$

The density variation due to the potential change can be written as :

$$\begin{aligned} \partial\rho(\mathbf{r}) &= \sum_{k}^{occ} f_k [\phi_{\mathbf{k}}^{(1)}(\mathbf{r})^2 - \phi_{\mathbf{k}}(\mathbf{r})^2] \\ &= \frac{4}{(2\pi)^6} \int_{q \neq 0} \tilde{V}(\mathbf{q}) e^{-i\mathbf{q}\cdot\mathbf{r}} \sum_{k}^{occ} \frac{f_k}{\mathbf{k}^2 - (\mathbf{k} - \mathbf{q})^2} d\mathbf{q} \end{aligned} \tag{3.162}$$

In Fourier space, f_k is the occupation number, depend on temperature according to Fermi-Dirac distribution, at zero temperature occupation number is 2.

$$\partial\tilde{\rho}(\mathbf{q}) = \frac{1}{(2\pi)^3} \tilde{V}(\mathbf{q}) \sum_{k}^{occ} \frac{f_k}{\mathbf{k}^2 - (\mathbf{k} - \mathbf{q})^2} \tag{3.163}$$

Compare this above equation with the definition of response function, we get

$$\tilde{\chi}_{lind}(\mathbf{q}) = \frac{1}{(2\pi)^3} \sum_{k}^{occ} \frac{f_k}{\mathbf{k}^2 - (\mathbf{k} - \mathbf{q})^2} \tag{3.164}$$

Setting the occupation number to 2(zero temperature case), replacing the summation with an integration, doing the integral in sperical coordinate, we can get :

$$\begin{aligned}
\tilde{\chi}_{lind}(\mathbf{q}) &= \frac{1}{(\pi)^3} \int_0^{2\pi} d\phi \int_0^{\pi} \sin\theta d\theta \int_0^{k_F} r^2 \frac{dk}{2qk\cos(\theta) - q^2} \\
&= -\frac{k_F}{(\pi)^2} \int_0^{k_F} k \ln|\frac{q+2k}{q-2k}| \\
&= -\frac{k_F}{(\pi)^2} (\frac{1}{2} + \frac{1-\eta^2}{4\eta} + \ln|\frac{1+\eta}{1-\eta}|)
\end{aligned} \tag{3.165}$$

where $\eta = q/(2 * k_F)$ is a diemnsionless momentum.

Extension to finite temperature T can be made by using the Fermi-Dirac distribution function for the occupation number. Unfortunately, the finite temperature lindhard function is not generally analytically solvable. However, it can be calculated numerically using

$$\tilde{\chi}_{lind}(\mathbf{q}, T) = \int_0^{\infty} dE \frac{\tilde{\chi}_{lind}(\mathbf{q}, , T = 0)}{4k_B T \cosh^2(\frac{E - \mu(T)}{2k_B T})} \tag{3.166}$$

Response function of TF and vW functionals

Using the same method, we can derive the response function of various kinetic energy density functionals, the zero temperature Thomas Fermi density functional is given by :

$$T_{TF}[\rho] = \frac{3}{10}(3\pi)^{2/3} \int \rho(\mathbf{r})^{5/3} d\mathbf{r} \tag{3.167}$$

The TF potential is calculated as :

$$\frac{\partial T_{TF}[\rho]}{\partial \rho(\mathbf{r})} = \frac{1}{2}(3\pi)^{2/3} \rho(\mathbf{r})^{2/3} d\mathbf{r} \tag{3.168}$$

Expand the $\rho(\mathbf{r})^{2/3}$ and keep the linear term,

$$\frac{\partial^2 T_{TF}[\rho]}{\partial \rho(\mathbf{r}) \partial \rho'(\mathbf{r})} = \frac{1}{3}(3\pi)^{2/3} \rho(\mathbf{r})^{-1/3} \tag{3.169}$$

So the response function is as following, $k_F = 3\pi^2 \rho(\mathbf{r}_0)$

$$\tilde{\chi}_{TF}(\mathbf{q}, T = 0) = -\frac{k_F}{\pi^2} \tag{3.170}$$

The response function of vW functional is

$$\tilde{\chi}_{vW}(\mathbf{q}, T = 0) = -\frac{k_F}{\pi^2} * \frac{4}{3q^2} \tag{3.171}$$

3.4.2 Lindhard dynamic response function $\omega \neq 0$

Definition :

$$\tilde{\chi}^{-1}_{Lind}(q,\omega) = -\mathcal{F}\Big(\frac{\partial^2 F[\rho(r)]}{\partial\rho(r)\partial\rho(r')}\Big) \tag{3.172}$$

We consider two approximate inverse response function for the NI-HEG (Non-Interacting Homogenous Electron Gas):

$$\tilde{\chi}^{-1}_{TFw}(q,\omega) = -\frac{(\pi)^2}{k_F}(\frac{1}{2} + \frac{3q^2}{4k_F^2} - \frac{3\omega^2}{k_F^2 q^2}) \tag{3.173}$$

$$\tilde{\chi}^{-1}_{CD}(q,\omega) = \tilde{\chi}^{-1}_{TFw}(q,\omega) + i\frac{\pi^3\omega}{k_F^2 q} \tag{3.174}$$

Potential Match :

$$T_{NI-HEG} = T_{TF} + T_{wW} + T_{NLR} + T_{CD} + T_{NLI} \tag{3.175}$$

Take derivative of both left and right hand sides with respect to ρ :

$$\frac{\partial T_{NI-HEG}(r,t)}{\partial \rho(r,t)} = \frac{\partial T_{TF}(r,t)}{\partial \rho(r,t)} + \frac{\partial T_{wW}(r,t)}{\partial \rho(r,t)} + \frac{\partial T_{NLR}(r,t)}{\partial \rho(r,t)} + \frac{\partial T_{CD}(r,t)}{\partial \rho(r,t)} + \frac{\partial T_{NLI}(r,t)}{\partial \rho(r,t)} \tag{3.176}$$

which is :

$$\tilde{\chi}^{-1}_{Lind}(q,\omega) = \tilde{\chi}^{-1}_{TF}(q,\omega) + \tilde{\chi}^{-1}_{vW}(q,\omega) + \tilde{\chi}^{-1}_{NLR}(q,\omega) + \tilde{\chi}^{-1}_{CD}(q,\omega) + \tilde{\chi}^{-1}_{NLI}(q,\omega) \tag{3.177}$$

Real Part of Lindhard :

$$Re[\tilde{\chi}_{Lind}(q,\omega)] = -\frac{k_F}{\pi^2}\left\{\frac{1}{2} - \frac{1-v_-^2}{4\bar{q}}\ln|\frac{v_-+1}{v_--1}| - \frac{1-v_+^2}{4\bar{q}}\ln|\frac{v_++1}{v_+-1}|\right\} \tag{3.178}$$

Imag Part of Lindhard :

$$Im[\tilde{\chi}_{Lind}(q,\omega)] = -\frac{k_F}{\pi^2}\left\{(1-v_-^2)\Theta[1-v_-^2] - (1-v_+^2)\Theta[1-v_+^2]\right\} \tag{3.179}$$

3.4.3 Dynamic kinetic energy functional from Lindhard response

Following previous section analysis leads to the current-dependent (CD) kinetic energy functional potential(KEDP, functional derivative of KEDF(White et al., 2018)). The functional was first developed by Alexander J. White from Los Alamos National Laboratory and published in (White et al., 2018). The current dependent functional is given as:

$$V_{CD}(\mathbf{r},t) = \frac{\pi^3}{2K_F^2(\mathbf{r},t)}\mathcal{F}_{q,r}^{-1}[i\mathbf{q}\cdot\mathbf{J}(\mathbf{q},t)/q](\mathbf{r}) \tag{3.180}$$

This term has been implemented in our TD-OF-DFT code to calculate stopping power. Comparison of response propagation between full Lindhard response, TFW response and TFW with new current dependent term are show as Fig. 3.1

Both response functions have a resonance point at $\frac{\omega}{k_F^2} = \frac{q}{k_F}\sqrt{\frac{1}{3} + (\frac{q}{2k_{f\,2}})}$, but the resonance is broadened by the imaginary part of the current dependent term. As mentioned in the paper(White et al., 2018), The real-time effect of the CD KEDP V_{CD} is then to dampen density oscillations introduced by the perturbation. In our case, it is the effect introduced by momentum transfer of the test particle.This dampening is caused by the decay of the bulk hydrodynamic motion into electron-hole excitation individual electron motions. In the TD-OF-DFT approach, these single-particle excitation are

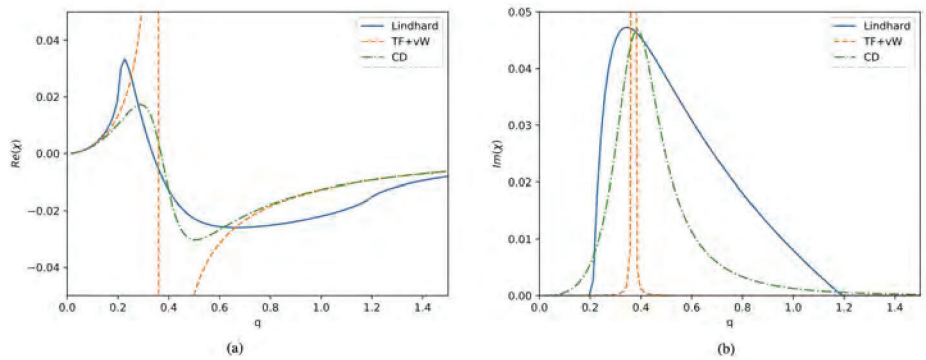

Figure 3.1: Dynamic density-density response functions for homogeneous electron gas as a function of wave vector (a) Real part of comparison (b) Imaginary part of comparison

resolved by the introduction of the auxiliary orbitals. The role of the CD KEDP is to effect these individual excitation.

3.4.4 Temperature-dependent dynamic kinetic energy functional

For previous section, the derivation of the current dependent is at zero temperature. For practical use of the simulation in warm dense matter, this term has to been extended to finite temperature case. In section 3.5.1, I mentioned that extension to finite temperature can be made using the Fermi-Dirac distribution function for the occupation number. Unfortunately, the finite temperature Lindhard function is not generally analytically solvable. However, it can be calculated numerically using

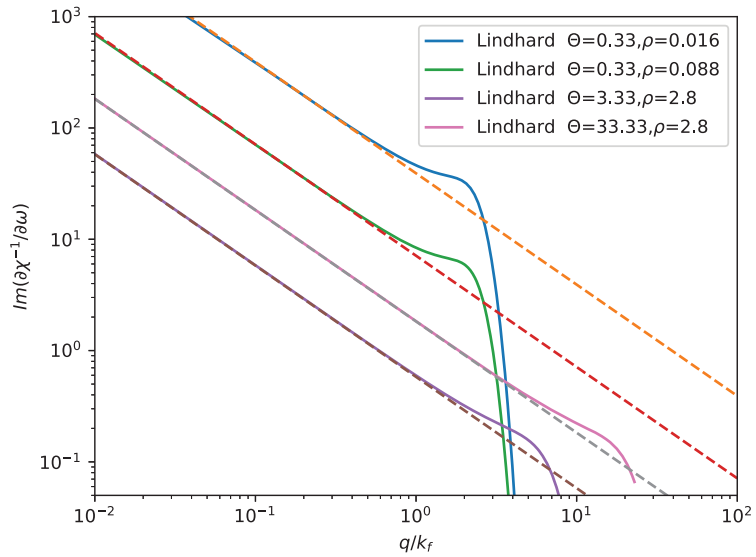

Figure 3.2: $Im(\partial\chi^{-1}/\partial\omega)$ as a function of the scaled momentum vector q/k_F.

$$\tilde{\chi}_{lind}(\mathbf{q}, T) = \int_0^\infty dE \frac{\tilde{\chi}_{lind}(\mathbf{q}, , T = 0)}{4k_B T \cosh^2(\frac{E - \mu(T)}{2k_B T})} \tag{3.181}$$

where $\mu(T)$ is the NI-HEG chemical potential. At high temperatures, $k_b T >> k_F^2/2$, when q goes to zero, we have

$$-i\frac{\partial\chi_L^{-1}(q, \omega = 0, T)}{\partial\omega} \approx -\frac{\pi^2}{k_F}[\frac{\pi}{2k_F q}] \times c_T \tag{3.182}$$

where $c_T = ([\Theta^{1/2} \times 1.69271]^{3.6} + 1)^{1/3.6}$. The two numerical constants are determined by fitting the $Im(\partial\chi^{-1}/\partial\omega)$ as a function of the scaled momentum vector q/k_F shown as Fig. 3.2. The temperature dependent CD potential is the product of the zero temperature current dependent term and

the temperature scaling constant c_t.

Chapter 4

Ab initio studies on the stopping power of warm dense matter with time-dependent orbital-free density functional theory

4.1 Experimental measure of stopping power

The experiment was conducted on OMEGA with a 532-μm-long solid Be plug, isochorically heated by x rays produced by a laser-irradiated Ag-coated CH tubeZylstra et al. (2015). A typical temperature of k_bT =32eV is inferred from XRTS in a similar experimental set upGlenzer et al. (2007). A D^3 Hellium glass capsule is imploded to generate the $\sim$ 15-MeV protons as the charged-particle source for probing the warm dense Be target. Once the protons passed through the Be target, the spectra of decelerated protons were recorded. At this condition $\rho = 1.78$ g/cm^3 and $k_bT = 32$ eV, the Be plasma is in its fluid phase with degeneracy and coupling parameter of $\theta \approx 2$ and $\Gamma \approx 0.3$.

4.2 Theoretical models of stopping power

4.2.1 Modified Li-Petrasso formalism

Li-Petrasso (Li and Petrasso, 1993*a*,*b*) proposed model of stopping power includes two parts, binary Coulomb collisions and collective plasma effects as

$$\frac{dE}{dx} = -(\frac{Z_t e}{v_t})^2 \omega_{pf}^2 \left[G(x^{t/f}) \ln\Lambda_b + \Theta(x^{t/f}) \ln(1.123\sqrt{x^{t/f}}) \right] \tag{4.1}$$

In the above equation, e is the fundamental charge, Z_t is the projectile charge in atomic units, v_t is the projectile travel velocity, ω_{pf} is the plasma frequency which are defined as

$$\omega_{pf} = \sqrt{\frac{4\pi n_f e_f^2}{m_f}} \tag{4.2}$$

where f represent different species for background particles, e_f is the charge of the field particle, n_f is the number density of particles and m_f is the mass. The term $x_{t/f} = \frac{v_t^2}{v_f^2}$ and $v_f^2 = \frac{2k_B T_f}{m_f}$. The last part of equation and also the most important part I want to mention is the Coulomb logarithm which is $\ln\Lambda_b$ in above expression. This term is generally written as

$$\ln\Lambda_b = \frac{1}{2}\ln\left[1 + (\frac{\lambda_D}{p_{min}}^2)\right] \tag{4.3}$$

For the Coulomb logarithm, λ_D is total Debye length both electrons and ions in the plasma since absolute screen length should be taken into account. It can be expressed as

$$\lambda_D = \frac{1}{\sqrt{\Sigma_f 4\pi n_f e_f^2/k_B T_f}} \tag{4.4}$$

The last term left is the maximum momentum transfer collision term which is defined Li-Petrasso paper as

$$p_{min} = \sqrt{p_v + (\frac{\hbar}{2m_r u})} \tag{4.5}$$

where $p_v = e_t e_f/m_r u_2$ is the classical impact parameter. And the second term is a correction term account for quantum effects. m_r is the reduced mass of test and field particles and u is the velocity ratio between test and background particles. Also in the paper Li and Patrosso notes that "in the low temperature, high density regime, electron quantum degeneracy effects must be considered in calculating maximum momentum transfer collision term and total Debye length". We can use effective field particle temperature to consider this quantum effects. In the next section, when compared the theoretical model with our simulation results, Li-Petrasso model is calculated in this way.

4.2.2 Brown-Preston-Singleton (BPS) model

The BPS (Brown, Preston and Singleton Jr, 2005*a*; Singleton Jr, 2008*a*) model describe the charged particle stopping effects in three parts, short-range Coulomb collisions, long-range dielectric response and quantum correction.The short-range classical energy loss term is given as

$$\begin{aligned}\frac{E^{CS}}{dx} =& \frac{e_t^2}{4\pi}\frac{\kappa_2}{m_t v_t}\sqrt{\frac{m_f}{2\pi\beta_f}}\int_0^1 du\sqrt{u}exp(-\beta_f m_f v_t^2 u/2) \\ & \left[-\ln(\beta_f\frac{e_t e_f K}{4\pi}\frac{m_f}{m_{tf}}\frac{u}{1-u}) + 2 - 2\gamma\right]\left[\beta_f M_{tf} v_t^2 - \frac{1}{u}\right] + \frac{2}{u}\end{aligned} \tag{4.6}$$

In above expression, f represent the field particle and t represent the projectile. e is particle charge, m is the mass of the particles, v_t is the particle velocity, $\kappa = \beta_f e_f^2 n_f$ is the Debye wave number for field species f.

The long-range dielectric response is given as

$$\begin{aligned}\frac{E^{CR}}{dx} =& \frac{e_t^2}{4\pi}\frac{i}{2\pi}\int_{-1}^1 duu\frac{\rho_f(uv_t)}{\rho_{tot}(uv_t)}F(uv_t)\ln(\frac{F(uv_t)}{K_2}) \\ & - \frac{e_t^2}{4\pi}\frac{i}{2\pi}\frac{1}{\beta_f m_t v_t^2}\left[F(v_t)\ln\frac{F(v_t)}{K_2} - F^*(v_t)\ln\frac{F^*(v_t)}{K_2}\right]\end{aligned} \tag{4.7}$$

The BPS model also include an quantum correction term. The BPS model used to compared with our simulation data is calculated using these three terms, short-range classical energy loss term, long range dielectric response term and quantum correction term. From this point of view, Li-Petrasso also

use three terms to describe full slowing effect of charged particles stopping in plasma or warm dense matter. In next section, we compared our model with theoretical models, the data is calculated from these equations. In their published papers, often the ionization level is calculated in more sophisticated way to take into effect of both free electrons and bound electrons. In these thesis, the calculation is only for model comparison purpose. An important point I want to emphasize here is that in our simulation model, we do not need any further assumptions of ionization level, the entire simulation system is self-consistence.

4.3 Simulation set up and Convergence Tests

Since we use plane wave in our simulation, the boundary condition is always periodic. This will give make the above derivation easier when we use plane wave. However, when we deal with dynamic case, the periodic boundary condition(PBC) will bring difficulties to us. Fig. 4.1 (a) is the example of our simulation unit with periodic boundary conditions. The middle box with highlight is the master box and other eight boxes are mirrored box. The figure shows us one test charges particle travel through uniform electron gas. We can clearly see the response of the background electron density. In the previous static case, we use Hellmann-Feynman theorem to calculate the force acting on the nucleus including the test particle since we treat the nucleus as classical particles. However, if we Hellmann-Feynman theorem

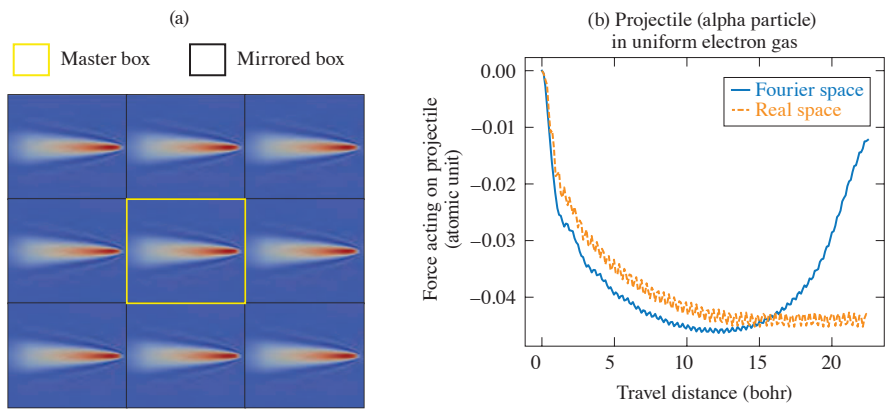

Figure 4.1: (a) Electron density profile of the simulation box include master box and mirrored box. We simulate the alpha particle travel through the uniform electron gas. (b) Force acting on the particle versus travel distance plot, the calculation is Fourier space is shown in blue and in real space is shown in orange.

to calculate the force in Fourier space, the effect of electron density will inevitably influence the momentum of the particle in master box. Fig. 4.1 (b) shows the force acting on the test particle along the way the particle travel through the simulation unit. The blue line shows the force calculating in Fourier space and the orange line shows the force calculating in real space. When the particle reach to the end of the simulation box, the particle will be influenced by the excited electron gas in the neighbor box, which is an artificial effect introduced by the periodic boundary condition. In real space we can calculate the force only consider the master box. The results are shown as the orange line in Fig. 4.1 (b). As the projectile travel through the box, the force acting on it will increase since the electron density will

accumulate around the test particle and provide the drag force. If the box is long enough, the particle will reach to a final steady state.

Note that the TD-OF-DFT method is all-electron and all-ion, treating the electronic structure of the whole system with the same level of theory. No partial- charge or bound vs free electrons need to be defined for the projectile or bulk ions. We use a range of 64 to 1024 atoms in a periodic rectangular box of up to 130 Ålength along the long side depend on the projectile velocity. The criterion to choose the box if make sure the test particle will reach to final steady state in uniform electron gas.

Convergence test is an essential step in numerical simulation especially in dynamic case. Simulation length scale, time scale and grid density plays an importance role in the calculation. We have tested to make sure box size, grid density, and time step are converged in our calculations. Fig.4.2 shows us the convege test on number of particles in the simulation unit. Fig.4.2 (a) indicate that when we increase the number of particles of the box and keep the density, the length of the box will increase and the force acting on the particle will gradually reach a steady state and the force will converge when the number of particle reach to a certain level. In this specific case, the *alpha* particle travel in the the uniform electron gas, we believe when number of particles in the box is larger than 150 the simulation is converged since the differences are within $\sim 4\%$ compared to larger boxes.

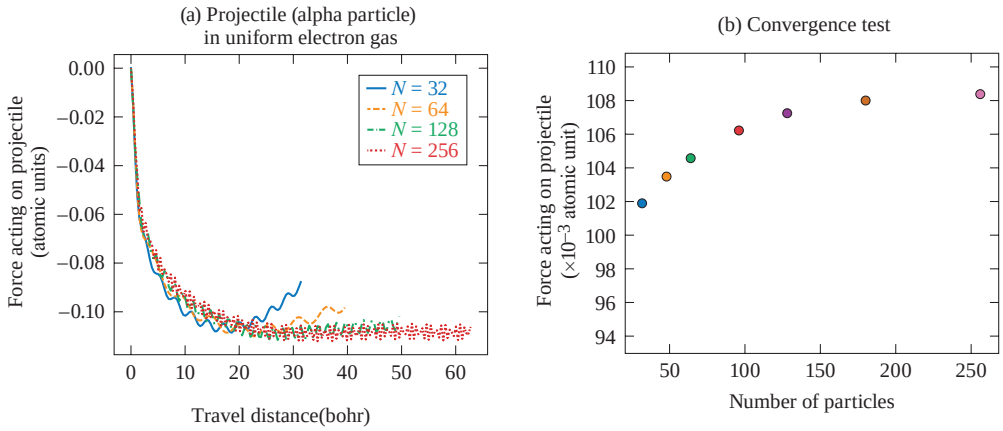

Figure 4.2: Convergence test of alpha particle travel through the uniform electron gas. (a) shows the force history along the path (b) shows the average force along the path

4.4 Proton Stopping in warm dense Beryllium

First we simulation one condition that is same as experimental measurement which is proton stopping in warm beryllium at temperature $k_bT = 32$ eV and solid density $= 1.78\text{g/cm}^3$. To start our TD-OF-DFT calculation we randomly take snapshots of the Be plasma as the initial condition, then launch the energetic testing proton to move across it. To illustrate, we show in Fig.4.3 the time-dependent electron densities on the x-y plane containing the test particle ($E_0 = 1.5$ MeV). The high-energy red spot represent locations of the background Be ions, while the proton(marked by white arrows) moves toward +x direction. One can see from the electron density profile that electron graduate accumulate around the test particle and the particle will generate the wave in front of the particle.

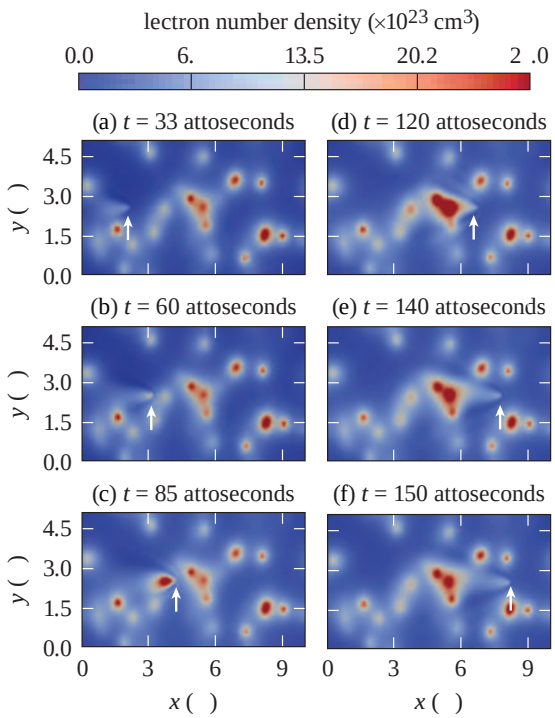

Figure 4.3: Snapshots of electron densities in an enlarged window on the x-y plane from TD-OF-DFT simulations of a 1.5-MeV proton traveling through a warm dense Be plasma of $k_bT = 32$ eV and solid density $= 1.78\text{g/cm}^3$.

While the test particle travel through the simulation unit, the drag force provided by the electron density will acting on the test particle slow the test particle down. We can easily track the energy change of the particle along the path and calculate the stopping power through $-dE/dx$. Fig. 4.4 shows the energy loss of the test particle versus the travel distance. The maximum travel distance in the example is up to 1.5 μm, the initial energy of the proton is 1.5MeV and loss $\sim$ 7keV long the path. The enlarged figure shows the energy fluctuations due to the variation of the electron density. However, the overall trend is energy loss. From this energy loss we can calculate the stopping power in this condition.

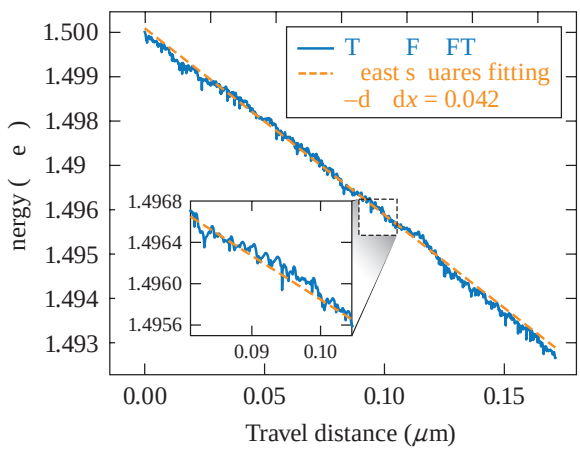

Figure 4.4: Test particle energy (proton) loss versus the travel distance in the simulation box. The initial energy is 1.5 MeV and travel up to 1.5 μm.

Launching TD-OF-DFT runs with different proton energies ranging from 2 to 15 MeV, we obtain the proton stopping power of the warm dense Be plasma. The converged results are shown in Fig.4.5(a). For each energy

point, we have statistically averaged over 20 snapshots from different plasma configurations. The error bar in Fig.4.5(a) represents the variation from the 20 different runs. Our results are compared to the three stopping-power models of LPLi and Petrasso (1993*a*), BPS Brown, Preston and Singleton Jr (2005*a*) Singleton Jr (2008*a*), and DF Clauser and Arista (2018) all with full electron density. For the exper- imentally accessible energy range, we provide a more- detailed comparison in the inset of Fig.4.5(b). The stopping power calculated by TD-OF-DFT is slightly lower than predictions of the LP model(blue solid line) and the BPS model((red dashed line) by $\sim 5\%$ and $\sim 11\%$ respectively, and higher than predicted by DF (orange dash-dotted line) by $\sim 20\%$.

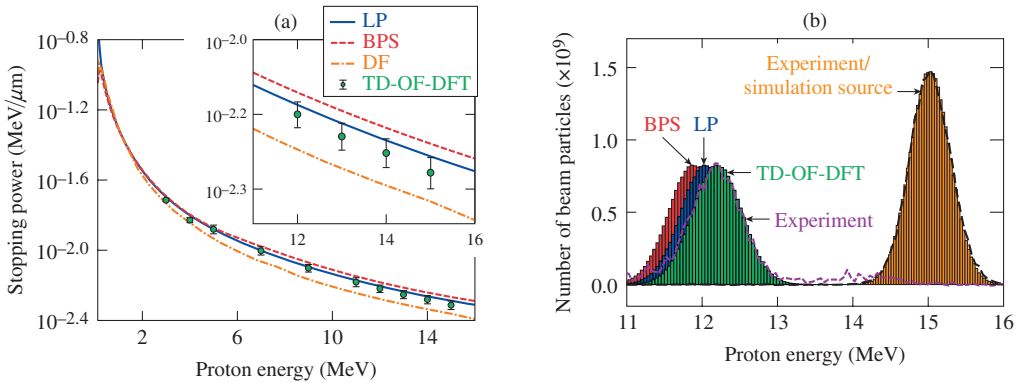

Figure 4.5: (a) The TD-OF-DFT calculated proton stopping power in high velocities (away from the Bragg peak) in comparison with three stopping-power models of LPLi and Petrasso (1993*a*), BPS Brown, Preston and Singleton Jr (2005*a*) Singleton Jr (2008*a*), and DF Clauser and Arista (2018). (b) Comparisons of the downshifted proton spectra among the experimental measurementsZylstra et al. (2015), predictions of LP and BPS models, and the TD-OF-DFT calculations

To directly compare with experimental measurements, we take the stopping-power results from TD-OF-DFT calculations and compute the energy spectrum after the protons have traversed the 532 μm Be target. The spectral comparisons between calculations and experiments are made in Fig.4.5(b). The proton source from the experiment is centered at $\sim$ 15 MeV as as shown by the black dashed line in Fig.4.5(b). After passing through the Be target, the protons are downshifted to a lower energy peaked near $E \sim$ 12.2MeV. For visual clarity we only plot the TD-OF-DFT, LP, and BPS spectra. The measured downshifted spectrum (purple long dashed line) is in good agreement with the TD-OF-DFT calculation (within $\sim$ 20keV), while both LP and BPS models predict somewhat larger downshifts than experiment. Namely, the proton peaks predicted by LP and BPS models are further downshifted by $\sim$ 100 and $\sim$ 200 keV, respectively, than both the experiment and the TD-OF-DFT calculation.

4.5 Alpha particle stopping in warm-dense DT

As a further example, we consider α particles stopping in warm-dense DT plasmas. To ultimately obtain experimental verification of stopping-power models, a uniform and well-characterized DT target is needed. On the other hand, we would like to have stopping power studies relevant to hot-spot and compressed DT-shell conditions in ICF. A possible solution is to scale the warm solid-density targets to have similar coupling and degeneracy parame-

ters to those of ICF ignition targets. To this end, we envision a 50-μm-thick solid DT slab at density $\rho = 0.25\text{g/cm}^3$ that can be isochorically heated to $k_bT = 10\text{eV}$ by laser produced soft x rays. At these conditions, we have a degeneracy parameter $\theta \approx 2.4$ and $\Gamma \approx 0.6$, which are close to the compressed DT-shell condition in ICF targets. With a DT-filled exploding-pusher target implosion, the α particles source can be generated separately for the stopping-power measurements. Bearing such an experimental scenario in mind, we have performed our TD-OF-DFT calculations with α particle energies ranging from 0.025 to 4MeV.

4.5.1 $\rho = 0.25\text{g/cm}^3$ and $k_bT = 10\text{eV}$

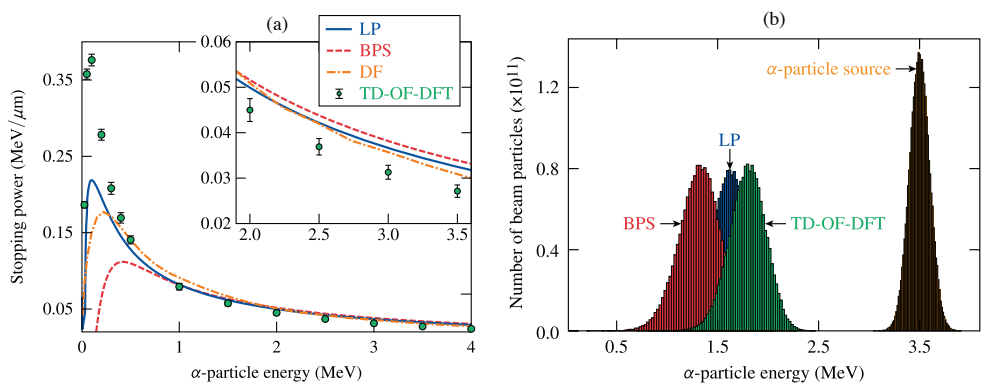

Figure 4.6: (a) The α-particle stopping power of warm dense DT plasma($\rho = 0.25\text{g/cm}^3$ and $k_bT = 10\text{eV}$) predicted by TD-OF-DFT calculations(green circles) compared to the LP, BPS and DF models(b) The calculated down-shifted spectra of α particles passing through the 50-μm DT slab at the same warm dense condition from both TD-OF-DFT simulations (green) and the two stopping power models (red and blue).

The simulation results are shown by Fig. 4.6(a). in which the LP, BPS, and DF models are also compared with our TD-OF-DFT calculations. Fig. 4.6(a) indicates that the stopping power from TD-OF-DFT calculations is smaller overall than LP, BPS, and DF models by $\sim 16\%$, $\sim 25\%$ and $\sim 15\%$. The TD-OF-DFT results predict greater stopping power than all the models near the Bragg peak. For such moderately coupled and partially degenerate plasmas, many-body effects become more difficult to account for in analytical models. Similar to the Be case, we also plot the spectral comparisons in Fig. 4.6(b) for the downshifted α-particle spectrum. The α-particle source has a central energy of $E_0 = 3.5$MeV with a thermal width of $\Delta E \approx 200$ keV. The downshifted α-particle spectra predicted by the LP model (blue) and the BPS model (red) peak at $E_{down} \approx 1.6$ MeV and $E_{down} \approx 1.3$ MeV, respectively. In contrast to these model predictions, our TD-OF-DFT calculations (green) give a downshifted peak at $E_{down} \approx 1.8$ MeV. These large differences between the stopping-power models and TD-OF-DFT calculations may readily facilitate experimental verifications since they significantly exceed the current experimental energy resolution ($\Delta E \sim 20$ to 50 keV).

4.5.2 $\rho = 0.25\mathbf{g/cm^3}$ and $k_bT = 50\mathbf{eV}$

Since plasma will undergo various condition during ICF explosion process, We also launch another calculation that simulate the DT condition that $\rho = 0.25\text{g/cm}^3$ and $k_bT = 50$eV. Under these conditions, the coupling parameter and degeneracy parameter which are close to the hot-spot conditions. The

target is still a 50-μm-thick solid DT slab that can be isochorically heated to $k_bT = 50$eV by laser produced soft x rays. The simulation results are shown by Fig. 4.7, in which the LP, BPS, and DF models are also compared with our TD-OF-DFT calculations. Similar to previous case, Fig. 4.7(a) indicates that the stopping power from TD-OF-DFT calculations is weaker overall than LP and BPS models by $\sim 13\%$. The TD-OF-DFT results predict greater stopping power than all the models near the Bragg peak which shift right compared with temperature $k_bT = 50$eV case. For such moderately coupled and partially degenerate plasmas, it is more difficult to account for many-body effects in analytical models. Similar to the previous DT case, we also plot the spectral comparisons in Fig. 4.7(b) for the downshifted α-particle spectrum. The α-particle source has a central energy of $E_0 = 3.5$MeV with a thermal width of $\Delta E \approx 200$ keV. The downshifted α-particle spectra predicted by the LP model (blue) and the BPS model (orange) peak at $E_{down} \approx 1.5$ MeV and $E_{down} \approx 1.3$ MeV, respectively. In contrast to these model predictions, our TD-OF-DFT calculations (green) give a downshifted peak at $E_{down} \approx 1.8$ MeV.

4.6 Proton stopping in warm Carbon

The slowing of energetic changed particles in warm dense matter is of great interest for not only numerical studies but also experimental probe. The research of stopping power is the path to explore of coupling and degen-

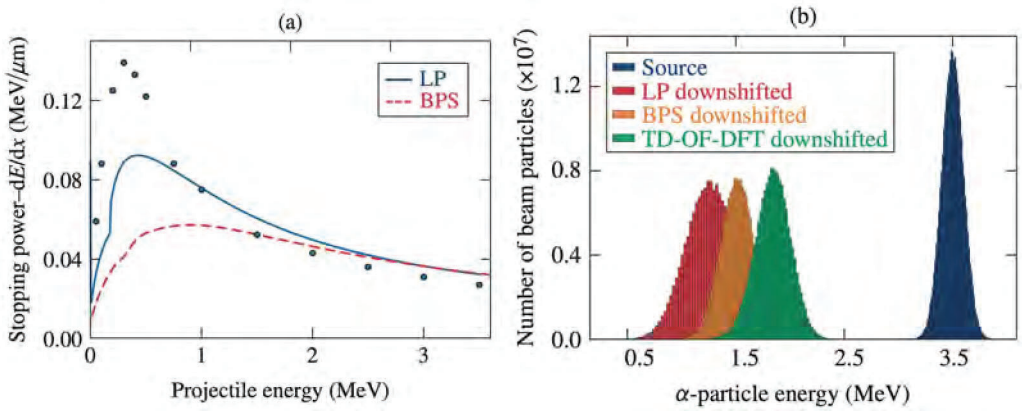

Figure 4.7: (a) The α-particle stopping power of warm dense DT plasma($\rho = 0.25\text{g/cm}^3$ and $k_bT = 50\text{eV}$) predicted by TD-OF-DFT calculations(green circles) compared to the LP and BPS(b) The calculated downshifted spectra of α particles passing through the 50-μm DT slab at the same warm dense condition from both TD-OF-DFT simulations (green) and the two stopping power models (red and orange).

eracy effects on the Coulomb interactions and also closely related to other charged particles transport properties such as thermal and electrical conductivity. Researches in LLE is planning precision experimental measurements of the stopping power of carbon on an isotropic source of monoenergetic 15-MeV protons. The experiments provides an opportunity to further verify our model under this specific case which is proton stopping in warm dense carbon. In our simulation, we are able to simulate the exact condition that experiment adopted. We use 300 μm-thick solid carbon slab at density $\rho = 0.25\text{g/cm}^3$ and $k_bT = 20\text{eV}$. The projectile particle which is proton in this case has the initial energy spectrum centered at 15 MeV.

The simulation results are shown by Fig. 4.8, in which our TD-OF-DFT

models are compared with LB and BPS models. In both LP and BPS models, we need to provide the electron number density to calculate the stopping power. In section 4.2, the derivation process of both models are revisited. Electron density plays an critical role in determining the accuracy of the models. In our comparisons we provide two limits of electron density, fully ionized as upper limit of stopping power and average ionization (average Z) as lower limit. Fig. 4.8(a) shows stopping power from TD-OF-DFT calculations comparing with LP and BPS models calculated using average ionization, in this case the value is 2.86. From the comparison we can clearly see that the stopping power calculated in this way is significantly lower than our TD-OF-DFT model.The reason behind it is that we neglect the effects of bound electrons. If we use fully ionized electron density to calculate the results are shown as Fig. 4.8 (b), in which we can find that both BPS and LP models predict high stopping power than out TD-OF-DFT simulations. I believe the reason behind it is also the ionization level. As least BGP and LP required accurate modeling of partial ionization to calcuate the stopping power. Our model could be used as one benchmark to infer the mean ionization potential used in theoretical plasma models. Similar to Be and DT case, we also plot the spectral comparison in Fig. 4.8 (c) for downshifted proton spectrum. The proton particle source has a central energy at energy of $E_0 = 15$ MeV with a thermal width of $\Delta E \approx 200$ keV. We plot the downshifted proton spectra predicted by LP model and BPS model in two ways. first use fully ionization model and the other one use average ionization. The downshifted

spectra predicted by our TD-OF-DFT model centered at 10.2 MeV while LP and BPS fully ionized model downshifted more at 9 MeV and 9.2 MeV and average Z downshifted less centering at 12.8 MeV.

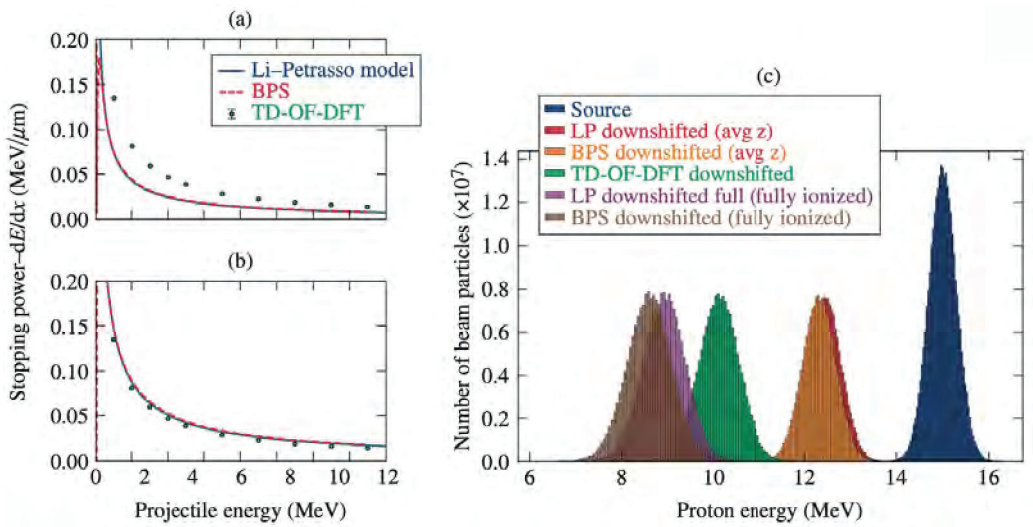

Figure 4.8: (a) The proton stopping power of Carbon plasma($\rho = 5.6\text{g/cm}^3$ and $k_bT = 20\text{eV}$) predicted by TD-OF-DFT calculations(green circles) compared to the LP and BPS models calculated using average ionization (b) The proton stopping power of Carbon plasma($\rho = 5.6\text{g/cm}^3$ and $k_bT = 20\text{eV}$) predicted by TD-OF-DFT calculations(green circles) compared to the LP and BPS models calculated using fully ionization electron density (c) The calculated downshifted spectra of proton particles passing through the 300-μm Carbon slab at the same warm dense condition from both TD-OF-DFT simulations (green) and the two stopping power models calculated using different ionization level

Bibliography

Baczewski, A. D., L. Shulenburger, M. P. Desjarlais, S. B. Hansen and R. J. Magyar. 2016. "X-ray Thomson Scattering in Warm Dense Matter without the Chihara Decomposition." *Phys. Rev. Lett.* 116:115004.

Benedict, Lorin X., Kevin P. Driver, Sebastien Hamel, Burkhard Militzer, Tingting Qi, Alfredo A. Correa, A. Saul and Eric Schwegler. 2014. "Multiphase equation of state for carbon addressing high pressures and temperatures." *Phys. Rev. B* 89:224109.

Betti, R and OA Hurricane. 2016. "Inertial-confinement fusion with lasers." *Nature Physics* 12(5):435.

Brown, Lowell S, Dean L Preston and Robert L Singleton Jr. 2005*a*. "Charged particle motion in a highly ionized plasma." *Physics Reports* 410(4):237–333.

Brown, Lowell S, Dean L Preston and Robert L Singleton Jr. 2005*b*. "Charged particle motion in a highly ionized plasma." *Physics Reports* 410(4):237–333.

Cauble, R., T. S. Perry, D. R. Bach, K. S. Budil, B. A. Hammel, G. W. Collins, D. M. Gold, J. Dunn, P. Celliers, L. B. Da Silva, M. E. Foord, R. J. Wallace, R. E. Stewart and N. C. Woolsey. 1998. "Absolute Equation-of-State Data in the 10–40 Mbar (1–4 TPa) Regime." *Phys. Rev. Lett.* 80:1248–1251.

Cayzac, W, A Frank, A Ortner, V Bagnoud, MM Basko, S Bedacht, C Bläser, A Blažević, S Busold, O Deppert et al. 2017. "Experimental discrimination of ion stopping models near the Bragg peak in highly ionized matter." *Nature communications* 8:15693.

Clauser, C. F. and N. R. Arista. 2018. "Stopping power of dense plasmas: The collisional method and limitations of the dielectric formalism." *Phys. Rev. E* 97:023202.

Clérouin, J. G. and S. Bernard. 1997. "Dense hydrogen plasma: Comparison between models." *Phys. Rev. E* 56:3534–3539.

Collins, L. A., S. R. Bickham, J. D. Kress, S. Mazevet, T. J. Lenosky, N. J. Troullier and W. Windl. 2001. "Dynamical and optical properties of warm dense hydrogen." *Phys. Rev. B* 63:184110.

Collins, L., I. Kwon, J. Kress, N. Troullier and D. Lynch. 1995. "Quantum molecular dynamics simulations of hot, dense hydrogen." *Phys. Rev. E* 52:6202–6219.

Desjarlais, Michael P. 2003. "Density-functional calculations of the liquid deuterium Hugoniot, reshock, and reverberation timing." *Phys. Rev. B* 68:064204.

Dittrich, Thomas R, SW Haan, MM Marinak, SM Pollaine, DE Hinkel, DH Munro, CP Verdon, GL Strobel, R McEachern, RC Cook et al. 1999. "Review of indirect-drive ignition design options for the National Ignition Facility." *Physics of Plasmas* 6(5):2164–2170.

Frenje, J. A., P. E. Grabowski, C. K. Li, F. H. Séguin, A. B. Zylstra, M. Gatu Johnson, R. D. Petrasso, V. Yu Glebov and T. C. Sangster. 2015. "Measurements of Ion Stopping Around the Bragg Peak in High-Energy-Density Plasmas." *Phys. Rev. Lett.* 115:205001.

Fu, Zhen-Guo, Zhigang Wang, Meng-Lei Li, Da-Fang Li, Wei Kang and Ping Zhang. 2016. "Dynamic properties of the energy loss of multi-MeV charged particles traveling in two-component warm dense plasmas." *Phys. Rev. E* 94:063203.

Glenzer, S. H., O. L. Landen, P. Neumayer, R. W. Lee, K. Widmann, S. W. Pollaine, R. J. Wallace, G. Gregori, A. Höll, T. Bornath, R. Thiele, V. Schwarz, W.-D. Kraeft and R. Redmer. 2007. "Observations of Plasmons in Warm Dense Matter." *Phys. Rev. Lett.* 98:065002.

Hu, S. X., B. Militzer, V. N. Goncharov and S. Skupsky. 2011. "First-principles equation-of-state table of deuterium for inertial confinement fusion applications." *Phys. Rev. B* 84:224109.

Hu, S. X., L. A. Collins, T. R. Boehly, J. D. Kress, V. N. Goncharov and S. Skupsky. 2014. "First-principles thermal conductivity of warm-dense deuterium plasmas for inertial confinement fusion applications." *Phys. Rev. E* 89:043105.

Hu, S. X., L. A. Collins, V. N. Goncharov, J. D. Kress, R. L. McCrory and S. Skupsky. 2015*a*. "First-principles equation of state of polystyrene and its effect on inertial confinement fusion implosions." *Phys. Rev. E* 92:043104.

Hu, S. X., L. A. Collins, V. N. Goncharov, J. D. Kress, R. L. McCrory and S. Skupsky. 2015*b*. "First-principles equation of state of polystyrene and its effect on inertial confinement fusion implosions." *Phys. Rev. E* 92:043104.

Hu, S. X., T. R. Boehly and L. A. Collins. 2014. "Properties of warm dense polystyrene plasmas along the principal Hugoniot." *Phys. Rev. E* 89:063104.

Kim, J., B. Qiao, C. McGuffey, M. S. Wei, P. E. Grabowski and F. N. Beg. 2015*a*. "Self-Consistent Simulation of Transport and Energy Deposition of Intense Laser-Accelerated Proton Beams in Solid-Density Matter." *Phys. Rev. Lett.* 115:054801.

Kim, J., B. Qiao, C. McGuffey, M. S. Wei, P. E. Grabowski and F. N. Beg. 2015*b*. "Self-Consistent Simulation of Transport and Energy Deposition of Intense Laser-Accelerated Proton Beams in Solid-Density Matter." *Phys. Rev. Lett.* 115:054801.

Krauser, William J, Nelson M Hoffman, Douglas C Wilson, Bernhard H Wilde, William S Varnum, David B Harris, Fritz J Swenson, Paul A Bradley, Steven W Haan, Stephen M Pollaine et al. 1996. "Ignition target design and robustness studies for the National Ignition Facility." *Physics of Plasmas* 3(5):2084–2093.

Li, Chi-Kang and Richard D. Petrasso. 1993*a*. "Charged-particle stopping powers in inertial confinement fusion plasmas." *Phys. Rev. Lett.* 70:3059–3062.

Li, Chi-Kang and Richard D. Petrasso. 1993*b*. "Charged-particle stopping powers in inertial confinement fusion plasmas." *Phys. Rev. Lett.* 70:3059–3062.

Liberman, David A. and Bard I. Bennett. 1990. "Atomic vibrations in a self-consistent-field atom-in-jellium model of condensed matter." *Phys. Rev. B* 42:2475–2484.

Magyar, Rudolph J, L Shulenburger and AD Baczewski. 2016. "Stopping of Deuterium in Warm Dense Deuterium from Ehrenfest Time-Dependent Density Functional Theory." *Contributions to Plasma Physics* 56(5):459–466.

More, RM, KH Warren, DA Young and GB Zimmerman. 1988. "A new quotidian equation of state (QEOS) for hot dense matter." *The Physics of fluids* 31(10):3059–3078.

Nellis, WJ, JA Moriarty, AC Mitchell and NC Holmes. 1997*a*. "Equation of state of beryllium at shock pressures of 0.4–1.1 TPa (4–11 Mbar)." *Journal of applied physics* 82(5):2225–2227.

Nellis, WJ, JA Moriarty, AC Mitchell and NC Holmes. 1997*b*. "Equation of state of beryllium at shock pressures of 0.4–1.1 TPa (4–11 Mbar)." *Journal of applied physics* 82(5):2225–2227.

Perrot, F. 1979. "Gradient correction to the statistical electronic free energy at nonzero temperatures: Application to equation-of-state calculations." *Physical Review A* 20(2):586.

Pierleoni, C., D. M. Ceperley, B. Bernu and W. R. Magro. 1994. "Equation of State of the Hydrogen Plasma by Path Integral Monte Carlo Simulation." *Phys. Rev. Lett.* 73:2145–2149.

Ragan, Charles E. 1982. "Shock compression measurements at 1 to 7 TPa." *Phys. Rev. A* 25:3360–3375.

Recoules, Vanina, Flavien Lambert, Alain Decoster, Benoit Canaud and Jean Clérouin. 2009. "Ab Initio Determination of Thermal Conductivity of Dense Hydrogen Plasmas." *Phys. Rev. Lett.* 102:075002.

Simakov, Andrei N, Douglas C Wilson, Sunghwan A Yi, John L Kline, Daniel S Clark, Jose L Milovich, Jay D Salmonson and Steven H Batha. 2014. "Optimized beryllium target design for indirectly driven inertial confinement fusion experiments on the National Ignition Facility." *Physics of Plasmas* 21(2):022701.

Singleton Jr, Robert L. 2008*a*. "Charged particle stopping power effects on ignition: Some results from an exact calculation." *Physics of Plasmas* 15(5):056302.

Singleton Jr, Robert L. 2008*b*. "Charged particle stopping power effects on ignition: Some results from an exact calculation." *Physics of Plasmas* 15(5):056302.

Singleton Jr, Robert L. 2008*c*. "Charged particle stopping power effects on ignition: Some results from an exact calculation." *Physics of Plasmas* 15(5):056302.

Tubman, Norm M., Elisa Liberatore, Carlo Pierleoni, Markus Holzmann and David M. Ceperley. 2015. "Molecular-Atomic Transition along the Deuterium Hugoniot Curve with Coupled Electron-Ion Monte Carlo Simulations." *Phys. Rev. Lett.* 115:045301.

White, Alexander J, Ondrej Certik, YH Ding, SX Hu and Lee A Collins. 2018. "Time-dependent orbital-free density functional theory for electronic stopping power: Comparison to the Mermin-Kohn-Sham theory at high temperatures." *Physical Review B* 98(14):144302.

Wilson, B, V Sonnad, P Sterne and W Isaacs. 2006. "Purgatorio—a new implementation of the Inferno algorithm." *Journal of Quantitative Spectroscopy and Radiative Transfer* 99(1-3):658–679.

Wilson, Douglas C, Paul A Bradley, Nelson M Hoffman, Fritz J Swenson, David P Smitherman, Robert E Chrien, Robert W Margevicius, DJ Thoma, Larry R Foreman, James K Hoffer et al. 1998. "The development and advantages of beryllium capsules for the National Ignition Facility." *Physics of Plasmas* 5(5):1953–1959.

Zylstra, A. B., J. A. Frenje, P. E. Grabowski, C. K. Li, G. W. Collins, P. Fitzsimmons, S. Glenzer, F. Graziani, S. B. Hansen, S. X. Hu, M. Gatu

Johnson, P. Keiter, H. Reynolds, J. R. Rygg, F. H. Séguin and R. D. Petrasso. 2015. "Measurement of Charged-Particle Stopping in Warm Dense Plasma." *Phys. Rev. Lett.* 114:215002.